

REPORT DOCUMENTATION PAGE			<i>Form Approved</i> <i>OMB No. 0704-0188</i>		
Public reporting burden for this collection of information is estimated to average 1 hour per response, including the time for reviewing instructions, searching existing data sources, gathering and maintaining the data needed, and completing and reviewing this collection of information. Send comments regarding this burden estimate or any other aspect of this collection of information, including suggestions for reducing this burden to Department of Defense, Washington Headquarters Services, Directorate for Information Operations and Reports (0704-0188), 1215 Jefferson Davis Highway, Suite 1204, Arlington, VA 22202-4302. Respondents should be aware that notwithstanding any other provision of law, no person shall be subject to any penalty for failing to comply with a collection of information if it does not display a currently valid OMB control number. PLEASE DO NOT RETURN YOUR FORM TO THE ABOVE ADDRESS.					
1. REPORT DATE (DD-MM-YYYY) 21-03-2008		2. REPORT TYPE Final Technical Report		3. DATES COVERED (From - To) From 01-01-2005 to 31-12-2007	
4. TITLE AND SUBTITLE Characterization and Prediction of Clear Air and Optical Stratospheric Turbulence for DOD High Altitude Platforms			5a. CONTRACT NUMBER		
			5b. GRANT NUMBER AFOSR FA 9550-05-1-0047		
			5c. PROGRAM ELEMENT NUMBER		
6. AUTHOR(S) Mahalov, Alex Nicolaenko, Basil			5d. PROJECT NUMBER		
			5e. TASK NUMBER		
			5f. WORK UNIT NUMBER		
7. PERFORMING ORGANIZATION NAME(S) AND ADDRESS(ES) Arizona State University Tempe, AZ 85287			8. PERFORMING ORGANIZATION REPORT NUMBER		
9. SPONSORING / MONITORING AGENCY NAME(S) AND ADDRESS(ES) Air Force Office of Scientific Research 875 North Randolph Road Arlington, VA 22203			10. SPONSOR/MONITOR'S ACRONYM(S) AFOSR		
			11. SPONSOR/MONITOR'S REPORT NUMBER(S)		
12. DISTRIBUTION / AVAILABILITY STATEMENT Unrestricted Public Availability and Release					
13. SUPPLEMENTARY NOTES					
14. ABSTRACT Stratospheric Clear Air Turbulence (CAT) is a major challenge to the safety, controllability and flight path optimization of the Global Hawk, Predator and other Unmanned Aerial Vehicles (UAVs) and Platforms. Optical Turbulence (OT) layers impact on the polarization and focusing of laser beams in communication systems and the Airborne Laser (ABL). The completed fundamental research project investigated the microscale physics of the upper troposphere/lower stratosphere (UTLS), closely correlating field measurements, high resolution numerical simulations and nonlinear mathematics to explicitly resolve multiscale turbulent dynamics of polarized inertia-gravity waves in the UTLS region. High performance massively parallel codes for the fully compressible, nonhydrostatic 3D Navier-Stokes equations and advanced data analysis tools for atmospheric characterization were developed and validated. High resolution coupled mesoscale/microscale simulations were carried out to characterize patchy, nonhomogeneous, shear-stratified UTLS turbulence under representative local atmospheric conditions (jetstream and topography). The embedded microscale nests and adaptive vertical gridding near the tropopause fully resolved laminated turbulent structures, with localized shear layers and stiff gradients of vertical velocity and potential temperature in the UTLS region.					
15. SUBJECT TERMS Atmospheric Turbulence, Optical Turbulence, Shear Stratified Flows, Optical Refractive Index Variability					
16. SECURITY CLASSIFICATION OF:			17. LIMITATION OF ABSTRACT	18. NUMBER OF PAGES	19a. NAME OF RESPONSIBLE PERSON Alex Mahalov
a. REPORT U	b. ABSTRACT U	c. THIS PAGE U			UU

FINAL REPORT

**CHARACTERIZATION AND PREDICTION OF CLEAR AIR AND OPTICAL
STRATOSPHERIC TURBULENCE FOR DoD HIGH ALTITUDE PLATFORMS**

AFOSR GRANT FA9550-05-1-0047

Alex Mahalov and Basil Nicolaenko
Principal Investigators
Department of Mathematics and Statistics
Department of Mechanical and Aerospace Engineering
Program in Environmental Fluid Dynamics
Arizona State University
Tempe, AZ 85287-1804
e-mail: mahalov@asu.edu, byn@stokes.la.asu.edu

1 Summary of Accomplishments

- Implementation on massively parallel architectures of the 3D Navier-Stokes Anelastic equations simulation codes; numerical algorithms based on operator splitting methods with rigorous error estimates and adaptive controls.
- Characterization of 3D dynamics of polarized inertia-gravity waves in patchy, non-Kolmogorov, nonhomogeneous turbulence in the Upper Troposphere/Lower Stratosphere (UTLS).
- Physical mechanism: dynamically unstable jet streams (around 10 -12 km) radiate polarized inertia-gravity waves into the lower stratosphere (15-25 km); large transfer of turbulent energy from the jet to the dispersive, polarized and non-monochromatic waves.
- The most unstable Kelvin-Helmholtz modes in the shear region are oblique and have preferred direction with respect to the background flow.
- Spectral characteristics of 3D strongly nonlinear gravity waves and effect of rotation; banded structure of cospectra is controlled by local shear and stratification.
- Spectral asymmetry in the spanwise direction caused by rotation and polarization.
- Propagation of polarized waves into the lower stratosphere (non-uniform background stratification): collapse of stability inside thin CAT layers.
- Rapid changes in direction of horizontal wind profiles (faster "corkscrew" in the hodograph) in thin layers in the lower stratosphere trigger instabilities and turbulence at altitudes determined by mesoscale conditions.
- Patchy vertical velocity with strong variation from $-10ms^{-1}$ to $+10ms^{-1}$ within few hundred meters in the horizontal, causing pitchroll instability for UAVs.
- Implementation on massively parallel architectures of nonhydrostatic fully compressible 3D Navier-Stokes equations for atmospheric dynamics: vertical nesting and adaptive gridding in coupled mesoscale/microscale codes.
- Lateral and upper boundary conditions in microscale nests: both upper and lateral boundary conditions are nudged within relaxation zones to the finest mesoscale nest fields using an operator splitting method.
- Characterization of patchy nonhomogeneous shear stratified UTLS turbulence under representative mesoscale conditions (jet streams and topography).
- High resolution microscale simulations of FASTEX, TREX and HAWAII campaigns of measurements.

- Embedded microscale nests and adaptive vertical gridding near the tropopause resolve laminated turbulent structures in real atmospheric conditions, with localized shear layers, stiff gradients of vertical velocity and sharp adiabatic layers in the UTLS region.
- Formation of counter gradient flows at fluctuating thin interfaces with sharp peaks of C_n^2 (peaks of C_n^2 at turbulent interfaces of adiabatic layers).
- Effective resolution of strong local variability across turbulent CAT and OT layers of the momentum and thermal eddy diffusivity coefficients, the Richardson number, the turbulent Prandtl number, and the refractive index structure function (C_n^2).

Technical Report

1 Theoretical and Computational Studies of Polarized Inertia-Gravity Waves in Stratified Nonhomogeneous Turbulence

1.1 New Findings: Physical Mechanisms

We have investigated nonlinear dynamics of gravity waves generated by Kelvin-Helmholtz instabilities in a nonhomogeneously stratified turbulence. For this purpose, a new formulation based on the divergence-vorticity form of the three dimensional Navier-Stokes anelastic equations in the presence of background rotation was developed (Mahalov et al 2007).

The model was then used to investigate waves radiated from a jet stream centered just below the tropopause under realistic background conditions. The turbulent mean velocity field was relaxed toward the background jet profile. In this context, in contrast to the unforced decaying case, a state is reached where the turbulence budgets are in quasi-equilibrium within the jet core. From the evolution of the averaged momentum flux above the jet, we found that gravity waves are continuously radiated once the quasi-equilibrium state is reached. The space-time spectral analysis performed at the upper flank of the jet shows a broad spectral band, with different phase speeds. The spectra obtained in the stratosphere above the jet core, evidence a shift toward lower frequencies and larger spatial scales compared to the spectra found along the jet flanks. The three dimensional character of the generated waves is identified using co-spectra of the spanwise and vertical velocities. The patterns of the co-spectra in the stratosphere exhibit two opposite poles of extrema; their signs demonstrate upward energy propagation. These extrema are found for spanwise wavenumbers different from zero, the signature of fully three-dimensional waves. The co-spectra at the upper flank of the jet show polarization which is opposite to that found at upper levels.

Effects of background rotation on the characteristics of the radiated waves were studied by including the Coriolis parameter. Rotation modifies the polarization relation between the horizontal wind components. These components are now out of phase. This behavior is evidenced by the hodograph of the horizontal wind vector, which follows an ellipse and rotates clockwise with altitude due to the upward energy propagation. Rotation breaks the symmetry of vw-cospectra in the spanwise direction and causes the co-spectra of the waves found at upper levels to be asymmetric in the spanwise, with negative wavenumbers prevailing in the co-spectra. In the presence of rotation, the most unstable modes along the jet flanks are oblique, and have a preferred direction in the spanwise. Without rotation, the oblique modes are present but they are not dominant. In the case with rotation, the oblique modes are dominant, even during the initial stages.

These results are in agreement with atmospheric measurements and the MU radar estimations of gravity wave enhancement and turbulent fluxes near the tropopause (Gavrilov and Fukao, 2004)

1.2 3D Anelastic Navier-Stokes Equations and Numerical Methods

The model used in our study was fully three dimensional weakly compressible Navier-Stokes equations with a background rotation, based on the anelastic approximation that filters the sound waves. This allows the governing equations to be integrated numerically using larger time steps. The model equations are written in the divergence-vorticity form:

$$\frac{\partial \eta}{\partial t} + u_0 \frac{\partial \eta}{\partial x} - \frac{\partial u_0}{\partial z} \frac{\partial w}{\partial y} + f\delta + N_\eta = D_M \Delta \eta \quad (1)$$

$$\frac{\partial \delta}{\partial t} + u_0 \frac{\partial \delta}{\partial x} + \frac{\partial u_0}{\partial z} \frac{\partial w}{\partial x} + \frac{\partial^2 \phi}{\partial x^2} + \frac{\partial^2 \phi}{\partial y^2} - f\eta + N_\delta = D_M \Delta \delta \quad (2)$$

$$\frac{\partial w}{\partial t} + u_0 \frac{\partial w}{\partial x} + \frac{\partial \phi}{\partial z} - g \frac{\theta}{\theta_0} + N_w = D_M \Delta w \quad (3)$$

$$\frac{\partial \theta}{\partial t} + u_0 \frac{\partial \theta}{\partial x} + N^2 \frac{\theta_0}{g} w + N_\theta = D_H \Delta \theta \quad (4)$$

$$\delta + \frac{1}{\rho_0} \frac{\partial(\rho_0 w)}{\partial z} = 0 \quad (5)$$

In these equations, each total field is separated in background and perturbations parts: $u_T = u_0(z) + u(x, y, z, t)$, $v_T = v(x, y, z, t)$, $w_T = w(x, y, z, t)$, $\theta_T = \theta_0(z) + \theta(x, y, z, t)$. The fields $\eta = v_x - u_y$, $\delta = u_x + v_y$, w and θ are the perturbations of the vertical component of vorticity, divergence of the horizontal velocities, vertical velocity and potential temperature, respectively; ϕ , u and v are perturbations of pressure, streamwise and spanwise velocities. $u_0(z)$, $\theta_0(z)$ and $\rho_0(z)$ are the background wind, potential temperature, and density which depend only on altitude; The parameter $N^2(z) = (g/\theta_0)(\partial\theta_0/\partial z)$ is the square of

Brunt-Väisälä frequency; f and g are the Coriolis parameter and the acceleration of gravity. D_M and D_H represent the kinematic and the thermal diffusion respectively. The nonlinear contributions from the perturbations are represented by $N_\eta = \partial N_v / \partial x - \partial N_u / \partial y$, $N_\delta = \partial N_u / \partial x + \partial N_v / \partial y$, N_w and N_θ , where $N_u = \text{div}(\rho_0 u \mathbf{u}) / \rho_0$, $N_v = \text{div}(\rho_0 v \mathbf{u}) / \rho_0$, $N_w = \text{div}(\rho_0 w \mathbf{u}) / \rho_0$, and $N_\theta = \text{div}(\rho_0 \theta \mathbf{u}) / \rho_0$.

The midlatitude jet maximum is typically below the tropopause, although the altitude of the tropopause may vary in the horizontal due to baroclinic effects (Lane et al. 2004). The numerical viscosity used in our simulations is adaptive since the vertical resolution is non-uniform in the vertical direction. It acts as a numerical smoother that damps perturbations with short wavelengths, typically twice the vertical grid spacing to avoid numerical instabilities.

A staggered grid mesh was used in the vertical, where the vertical velocity, potential temperature are represented at a common grid point (p); and the pressure, divergence and vorticity are displaced half a grid interval from that point ($p+1/2$). This arrangement improves the resolution without reducing the time step. The numerical scheme used is semi-implicit, second-order accurate in time. The advective terms in the nonlinear contributions from the perturbations were computed by using the leapfrog scheme and the Runge-Kutta 3rd order scheme. The discretizations of the equations in the horizontal spectral space are given by:

$$\begin{aligned} & \frac{\eta_{p+1/2}^{n+1} - \eta_{p+1/2}^{n-1}}{2dt} + jku_{0,p+1/2} \frac{\eta_{p+1/2}^{n+1} + \eta_{p+1/2}^{n-1}}{2} \\ & - jlu_{0z,p+1/2} \frac{w_{p+1/2}^{n+1} + w_{p+1/2}^{n-1}}{2} + f \frac{\delta_{p+1/2}^{n+1} + \delta_{p+1/2}^{n-1}}{2} = -N_\eta^n \end{aligned} \quad (6)$$

$$\begin{aligned} & \frac{\delta_{p+1/2}^{n+1} - \delta_{p+1/2}^{n-1}}{2dt} + jku_{0,p+1/2} \frac{\delta_{p+1/2}^{n+1} + \delta_{p+1/2}^{n-1}}{2} \\ & + jku_{0z,p+1/2} \frac{w_{p+1/2}^{n+1} + w_{p+1/2}^{n-1}}{2} - f \frac{\eta_{p+1/2}^{n+1} + \eta_{p+1/2}^{n-1}}{2} - K^2 \phi_{p+1/2} = -N_\delta^n \end{aligned} \quad (7)$$

$$\begin{aligned} & \frac{w_p^{n+1} - w_p^{n-1}}{2dt} + jku_{0,p} \frac{w_p^{n+1} + w_p^{n-1}}{2} + \frac{S_p}{ds} (\phi_{p+1/2} - \phi_{p-1/2}) \\ & - \frac{g}{\theta_{0,p}} \frac{\theta_p^{n+1} + \theta_p^{n-1}}{2} = -N_w^n \end{aligned} \quad (8)$$

$$\frac{\theta_p^{n+1} - \theta_p^{n-1}}{2dt} + jku_{0,p} \frac{\theta_p^{n+1} + \theta_p^{n-1}}{2} + \frac{\theta_{0,p}}{g} N_p^2 \frac{w_p^{n+1} + w_p^{n-1}}{2} = -N_\theta^n \quad (9)$$

$$\delta_{p+1/2}^{n+1} + \frac{S_{p+1/2}}{ds \rho_{0,p+1/2}} (\rho_{0,p+1} w_{p+1}^{n+1} - \rho_{0,p} w_p^{n+1}) = 0 \quad (10)$$

The function $S(z)$ in the continuity equation (10) is introduced for the stretching. The equations are written using uniform grid spacing (ds) in the new vertical variable s , which give a stretched grid spacing in z . The grid spacing in both grids are linked by the relation

$ds = S(z)dz$, where $S(z) = (\partial s / \partial z)$. By putting the unknown variables in the left hand side, equations (6), (7), (8) and (9) can be written as:

$$C_{p+1/2}\eta_{p+1/2}^{n+1} + fdt\delta_{p+1/2}^{n+1} - jlu_{0z,p+1/2}dtw_{p+1/2}^{n+1} = F_\eta \quad (11)$$

$$C_{p+1/2}\delta_{p+1/2}^{n+1} - fdt\eta_{p+1/2}^{n+1} + jku_{0z,p+1/2}dtw_{p+1/2}^{n+1} - 2dtK^2\phi_{p+1/2} = F_\delta \quad (12)$$

$$C_p w_p^{n+1} - \frac{g}{\theta_{0,p}} dt\theta_p^{n+1} + dt\frac{S_p}{ds}(\phi_{p+1/2} - \phi_{p-1/2}) = F_w \quad (13)$$

$$C_p\theta_p^{n+1} + \frac{\theta_{0,p}}{g}N_p^2dtw_p^{n+1} = F_\theta \quad (14)$$

where,

$$\begin{aligned} F_\eta &= -2dtN_\eta^n + C_{0,p+1/2}\eta_{p+1/2}^{n-1} - fdt\delta_{p+1/2}^{n-1} + jlu_{0z,p+1/2}dtw_{p+1/2}^{n-1} \\ F_\delta &= -2dtN_\delta^n + C_{0,p+1/2}\delta_{p+1/2}^{n-1} + fdt\eta_{p+1/2}^{n-1} - jku_{0z,p+1/2}dtw_{p+1/2}^{n-1} \\ F_w &= -2dtN_w^n + C_{0,p}w_p^{n-1} + (g/\theta_{0,p})dt\theta_p^{n-1} \\ F_\theta &= -2dtN_\theta^n + C_{0,p}\theta_p^{n-1} - N_p^2(\theta_{0,p}/g)dtw_p^{n-1}, \end{aligned}$$

where $C = 1 + jku_0dt$, $C_0 = 1 - jku_0dt$, and $K^2 = k^2 + l^2$. Using (11) and (12) to eliminate $\eta_{p+1/2}^{n+1}$, and (13) and (14) to eliminate θ_p^{n+1} , the following equations are derived:

$$A_{p+1/2}\delta_{p+1/2}^{n+1} + D_{p+1/2}w_{p+1/2}^{n+1} - 2dtC_{p+1/2}K^2\phi_{p+1/2} = C_{p+1/2}F_\delta + fdtF_\eta \quad (15)$$

$$B_p w_p^{n+1} + 2dtC_p\frac{S_p}{ds}(\phi_{p+1/2} - \phi_{p-1/2}) = C_p F_w + \frac{g}{\theta_{0,p}} dtF_\theta \quad (16)$$

where, $A = C^2 + (fdt)^2$, $B = C^2 + (Ndt)^2$, and $D = jdtu_{0z}(Ck - lfdt)$. The pressure terms ϕ are then eliminated by evaluating (15) at $p + 1/2$ and $p - 1/2$, and using (16):

$$\begin{aligned} \frac{C_p S_p}{ds} \left\{ \frac{A_{p+1/2}}{C_{p+1/2}} \delta_{p+1/2}^{n+1} - \frac{A_{p-1/2}}{C_{p-1/2}} \delta_{p-1/2}^{n+1} + \frac{D_{p+1/2}}{C_{p+1/2}} w_{p+1/2}^{n+1} - \frac{D_{p-1/2}}{C_{p-1/2}} w_{p-1/2}^{n+1} \right\} \\ + K^2 B_p w_p^{n+1} = Q_p \quad (17) \end{aligned}$$

$$Q_p = \frac{C_p S_p}{ds} \left\{ F_{\delta,p+1/2} - F_{\delta,p-1/2} + fdt \left(\frac{F_{\eta,p+1/2}}{C_{p+1/2}} - \frac{F_{\eta,p-1/2}}{C_{p-1/2}} \right) \right\} + K^2 \left(C_p F_{w,p} + \frac{g}{\theta_0} dt F_{\theta,p} \right).$$

Using (17) and the continuity equation, and by defining $\psi_p^{n+1} = \rho_0 w_p^{n+1}$, with $w_{p+1/2} = (w_p + w_{p+1})/2$, the following equations are obtained:

$$\begin{aligned} (\alpha_p + \gamma_p^1) \psi_{p-1}^{n+1} + (\beta_p - \gamma_p^2) \psi_{p+1}^{n+1} - \left(\alpha_p + \beta_p + \gamma_p^2 - \gamma_p^1 + \frac{B_p}{A_p} K^2 \right) \psi_p^{n+1} = \\ -Q_p \frac{\rho_{0,p}}{A_p} \quad (18) \end{aligned}$$

where

$$\begin{aligned}\alpha_p &= \frac{C_p}{C_{p-1/2}} \frac{\rho_{0,p}}{\rho_{0,p-1/2}} \frac{A_{p-1/2}}{A_p} \frac{S_p S_{p-1/2}}{ds^2} \\ \beta_p &= \frac{C_p}{C_{p+1/2}} \frac{\rho_{0,p}}{\rho_{0,p+1/2}} \frac{A_{p+1/2}}{A_p} \frac{S_p S_{p+1/2}}{ds^2} \\ \gamma_p^1 &= \frac{1}{2} \frac{C_p}{C_{p-1/2}} \frac{\rho_{0,p}}{\rho_{0,p-1/2}} \frac{D_{p-1/2}}{A_p} \frac{S_p}{ds} \\ \gamma_p^2 &= \frac{1}{2} \frac{C_p}{C_{p+1/2}} \frac{\rho_{0,p}}{\rho_{0,p+1/2}} \frac{D_{p+1/2}}{A_p} \frac{S_p}{ds}.\end{aligned}$$

The difference equation (18) was solved with the boundary conditions $\psi = \rho_0 w = 0$ at the top and the bottom vertical levels, then θ , δ and η are updated using (14), (10) and (11). The numerical code was fully parallelized using MPI, and the memory used by the code was optimized so that a number of processors as small as possible is used to achieve desired resolution. The accuracy of the numerical simulation results was confirmed by doubling the numerical resolutions to resolve the fully nonlinear 3D dynamics, and comparing with the lower resolution runs.

Our numerical code is different from the conventional ones where an elliptic equation is derived for the pressure, and solved at each time step. In these methods, it is usually necessary to add a velocity corrector at the end of each time step so that this field satisfies the continuity equation. In our numerical scheme, the pressure equation is not used. Instead, the continuity equation is used directly, and corrections to the velocity field are not required since the continuity equation is satisfied automatically at the end of each time step. This allows to derive finite difference equations for the vertical velocity Eq (18), for which the boundary conditions are imposed, rather than the pressure.

1.3 Spectral characteristics of 3D strongly nonlinear gravity waves and effect of rotation

Interaction of gravity waves with the tropopause and their amplification in the lower stratosphere are three-dimensional phenomena. In particular, the typical N^2 -notch profile of Brunt-Vaisala frequency observed in the tropopause region drastically effects the transmission of gravity waves into the lower stratosphere (Joseph et al 2004).

We used the technique of space-time spectral analysis presented for example in Moustououi et al. (2004). In order to reduce spectral leakage, the temporal series have been tapered by Welch windows. Figure 1 shows cospectra of streamwise and the vertical velocities (U,W) at 24 km in the stratosphere and at the upper flank of the jet (14.3 km), where $Co(U, W) = Real(UW^*)$. U, V and W denote Fourier transforms in time and space for u, v and w respectively. In the upper flank of the jet (Fig. 1b), the cospectrum is dominated by eastward propagating perturbations ($k_x \geq 0$). Also, the cospectrum shows a presence

of polychromatic modes, which are organized in a spectral band that do not cross the origin ($k=0$), indicating the presence of different phase speeds. This shape is determined by the local mean flow and background stratification, which allows the presence of wavenumbers and frequencies within the above spectral band only. This is confirmed by analysis of the Taylor-Goldstein equation. Away from the jet core (in the stratosphere), the spectrum shows a shift toward lower frequencies and smaller wavenumbers (Fig. 1a). The high frequencies and smaller wavenumbers found in the spectra in the upper flank of the jet are largely dominated by shear induced turbulence/mixing layer dynamics where the flow is unstable. In the presence of different phase speeds, however, as in the present case, it is possible for waves to be present in the shear region and above the shear region with similar wavenumber but with a shifted frequency (Fig. 1). The shift in time frequency is produced by local changes of the total mean wind ($u_T(z, t) = \bar{u}(z, t) + u_0(z)$), and the stratification. The most unstable modes, that are excited in the shear region because of the presence of the mean wind, have high frequencies, and are prevented from propagating into the stratosphere where the mean wind is equal to zero since their frequencies are higher than the Brunt-Vaisala frequency. However, these modes excite other modes through nonlinear interactions, including low frequency modes for which time frequency is below the Brunt-Vaisala frequency, and consequently, these waves are able to propagate into the stratosphere. The effectiveness of the envelope radiation mechanism, when applied to time frequency, has been demonstrated by Babin et al. (1998, 2002).

Figure 2 shows cospectra of (V,W) as a function of the streamwise and the spanwise wavenumbers in the stratosphere (Fig. 2a) and in the upper flank of the jet (Fig. 2b). Cospectra of (V,W) are useful to characterize 3D modes or waves, because the contribution to these spectra is dominated by the waves that have spanwise structures, and thus are completely ignored in 2D studies. The presence of 3D waves is evident from Fig. 2, which shows maxima at spanwise wavenumbers different from zero in both levels. The cospectrum of (V,W) at the upper flank of the jet (Fig. 2b) shows opposite polarization compared to that found in the stratosphere around 24 km, even if the cospectrum of (U,W) is also positive in this region. Kelvin Helmholtz instability need to be taken into account to explain this opposite polarization. In the stratosphere, the polarization is consistent with wave energy propagating upward; while in the upper flank of the jet, the polarization is due to both locally growing instability and negative shear. In the lower flank of the jet, the polarization changes again because the shear is positive in this region.

The role of a background rotation on the generated gravity waves was investigated. Simulations were conducted using the same background and initial conditions as those described above, but with a nonzero Coriolis parameter f . Figure 3 shows a hodograph of the horizontal wind at a given horizontal location between altitudes of 18 km and 25 km. In the presence of rotation (Fig. 3b), the hodograph approximately describes an ellipse. The horizontal wave vector rotates clockwise with altitude, which indicates that the vertical group velocity is pointing upward. This is further confirmation that the waves are radiated from the jet. The inertia gravity waves can induce local lateral shear due to the change of the horizontal wind direction with height (Cot and Barat, 1986), resulting in formation of local mixing layers. Some local layers with high local shear and low stability are found just

above the upper flank of the jet where the resolution is still sufficient to resolve such layers.

Figure 4 shows the amplitude of cospectra of (V,W) at 24 km as a function of time frequency and the spanwise wavenumber. In the case where rotation is not included (Fig. 4a), the cospectra is almost symmetric in the spanwise direction. For parallel flow, three dimensional waves with wave vectors that form an angle with respect to the streamwise can be generated, but these waves are symmetric in the spanwise. The small spanwise asymmetry seen in the cospectrum of (V,W) (Fig 4a) is due to asymmetries in initial conditions. When rotation is included, however, a strong asymmetry is found in the spanwise (Fig. 4b), with negative spanwise wavenumber dominating the spectrum. The asymmetry found in the spanwise direction is a robust feature and is not an artifact due to asymmetry in the initial conditions. To further confirm this, two simulations with and without rotation were conducted, using initial conditions with the constraint of evenness in the spanwise modes, so that no spanwise asymmetry is introduced at the beginning of the simulations. Vertical and the spanwise velocity fields were stored for each vertical level and at each time interval of 40 s. Then, each field was decomposed into two fields by separating positive and negative spanwise wavenumbers. Finally, the contributions from each of these fields to the momentum flux of (V,W) were calculated at each vertical level. In both cases, the contributions are from wavevectors with $k_y \neq 0$, thus, only three dimensional modes or waves are involved. For the case where rotation is not included, the contributions from positive and negative spanwise directions are exactly symmetric. When rotation is included, contribution to the momentum flux of modes with negative wavenumbers are dominating. This occurs not only at stratospheric levels, but also within the jet region. Our results demonstrated that in the presence of rotation, the most unstable modes in the shear region are oblique and have preferred direction with respect to the background flow. This fully 3D phenomenon cannot be described by 2D analysis.

The dynamics of nonlinear wave-turbulence interactions were investigated using very high resolution ($2048 \times 2048 \times 1024$) simulations of quasi-stratified turbulence induced by a broad (3 km) jet centered at 11 km , partly straddling the tropopause at $z = 12 \text{ km}$. The mean flow was relaxed to the background mesoscale jet. As turbulence due to stratified shear flow is in its active stage, the Brunt-Vaisala profile develops asymmetric "notch" structures; these are typical of the tropopausal region and delineate a layer of strong turbulent mixing.

The cross section of the Richardson number and the shear in the jet region (Figure 5) evidenced strong Kelvin-Helmholtz instabilities (gradient Richardson number $R_{ig} < 0.25$) on both upper and lower flanks of the jet, with local patches of strong shear turbulence. Of special interest are "fingers" of low (< 0.25) R_{ig} pointing into the stratosphere between $z = 12 \text{ km}$ and $z = 13 \text{ km}$; these are the signature of unstable gravity waves radiated away from the top of the turbulent layer into the lower stratosphere. Such 'fingers' and 'pockets' of well mixed air penetrate the strongly stratified stratospheric levels beyond 13 km ; and, alternatively, patches with larger values are observed penetrating the lower stratified troposphere down to 12 km . Such fingers are manifestation of mixing dynamics at the edges of shear-induced turbulent layer, which excite and radiate inertia-gravity waves

as evidenced by the penetration of these fingers above and below the flanks of the jet.

We found that the wave radiation into the stratosphere is produced by two different mechanisms. One is the nonlinear interaction between modes within the shear layer that excites lower frequencies and wavenumbers, which can escape upward. The other is the penetration of low Richardson number fingers above the shear layer where waves are generated locally by local shear or even convective instability. These fingers act like pulses that locally displace isentropes, resulting in wave radiation by the restoring forces due to high stratification in the lower stratosphere. The vertical propagation of such waves is demonstrated in Figure 6, i.e. x - z cross-sections for vertical velocity w and potential temperature (turbulent mean + fluctuations, background removed). Such waves are radiated away from the jet and act to transport the energy and the momentum flux away from it. There is a *large transfer of turbulent energy from the jet to dispersive, polarized and non-monochromatic inertia-gravity waves*. This is confirmed by the space-time spectral analysis of such wave packets. Streamwise, spanwise and time-frequency cospectra were computed at different vertical levels. Figure 7 shows cospectrum of spanwise v and vertical w velocities $Co(V, W) = Real(VW^*)$ at $z = 11.5km$, on the upper flank of the jet. ω is the frequency and k_y the spanwise wavenumber; cospectra are averaged along the streamwise wavenumber. In Figure 7, maxima at spanwise wavenumbers different from zero confirm such 3D structures. Strong asymmetry towards negative spanwise wavenumbers reflects the impact of weak rotation on the transmission and radiation of these waves from the upper flank of the jet into the strongly stably stratified lower stratosphere. The wave packets are mostly high frequency, small wavelength ($5km$ streamwise and $15km$ spanwise), reflecting the primary oblique unstable modes of the Kelvin-Helmholtz billows on the upper flank of the jet. *Indeed, the most unstable Kelvin-Helmholtz modes in the shear region are oblique and have preferred direction with respect to the background flow*. The cospectrum $Co(V, W)$ in the stratosphere at $20km$ (Figure 8) shows striking changes as the wave packet propagates upward: peaks are shifted to lower frequencies and smaller wavenumbers (larger scales); similar shifts are observed for $Co(U, W)$. There is still asymmetry toward negative spanwise wavenumbers, the signature of weak rotation and polarization of these inertia-gravity (IG) waves. The marked shift towards larger horizontal scales (with higher altitude) and the polarization are associated with helical horizontal winds along these propagating I-G waves rotating clockwise with higher altitude in a "corkscrew" helicoidal motion.

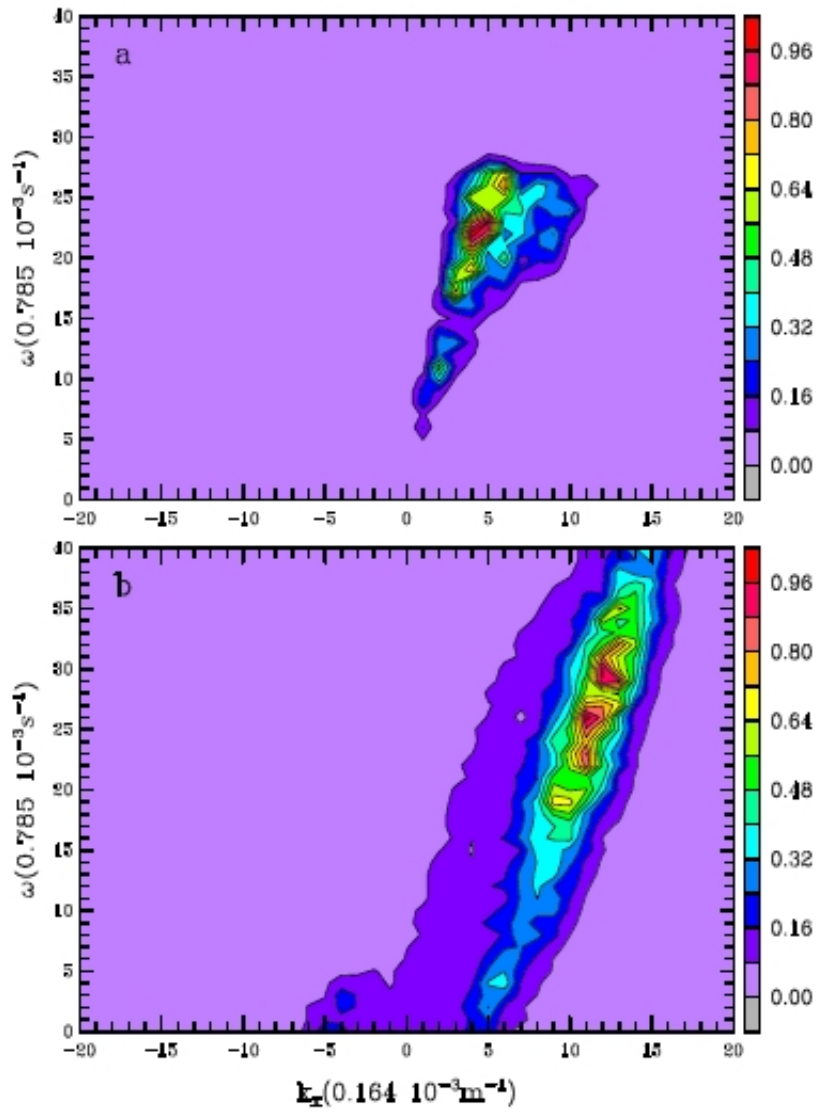


Figure 1: Normalized co-spectra of (U,W), averaged over the spanwise wavenumbers at $z=24$ km (a), and at the upper flank of the jet (b).

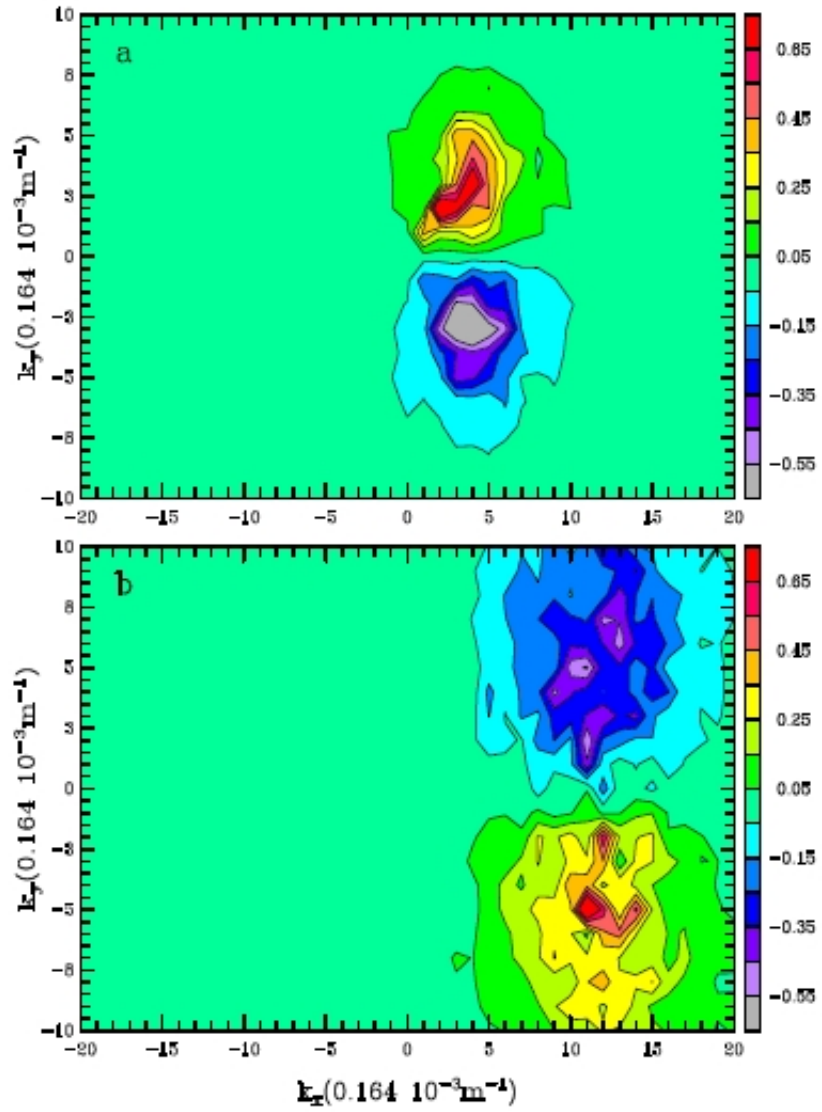


Figure 2: Normalized co-spectra of (V,W), averaged over the time frequency at $z=24$ km (a), and at the upper flank of the jet (b).

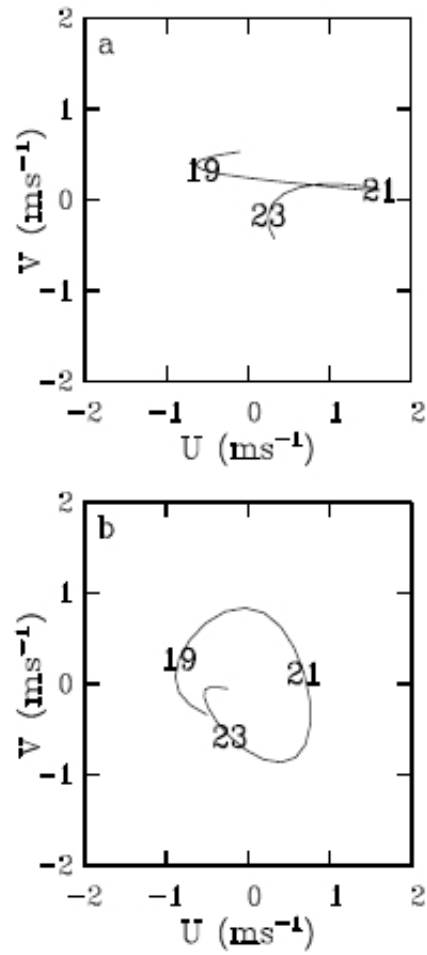


Figure 3: Hodograph of the horizontal wind between 18 km and 25 km without rotation (a) and with rotation (b). The numbers indicate the altitude in (km).

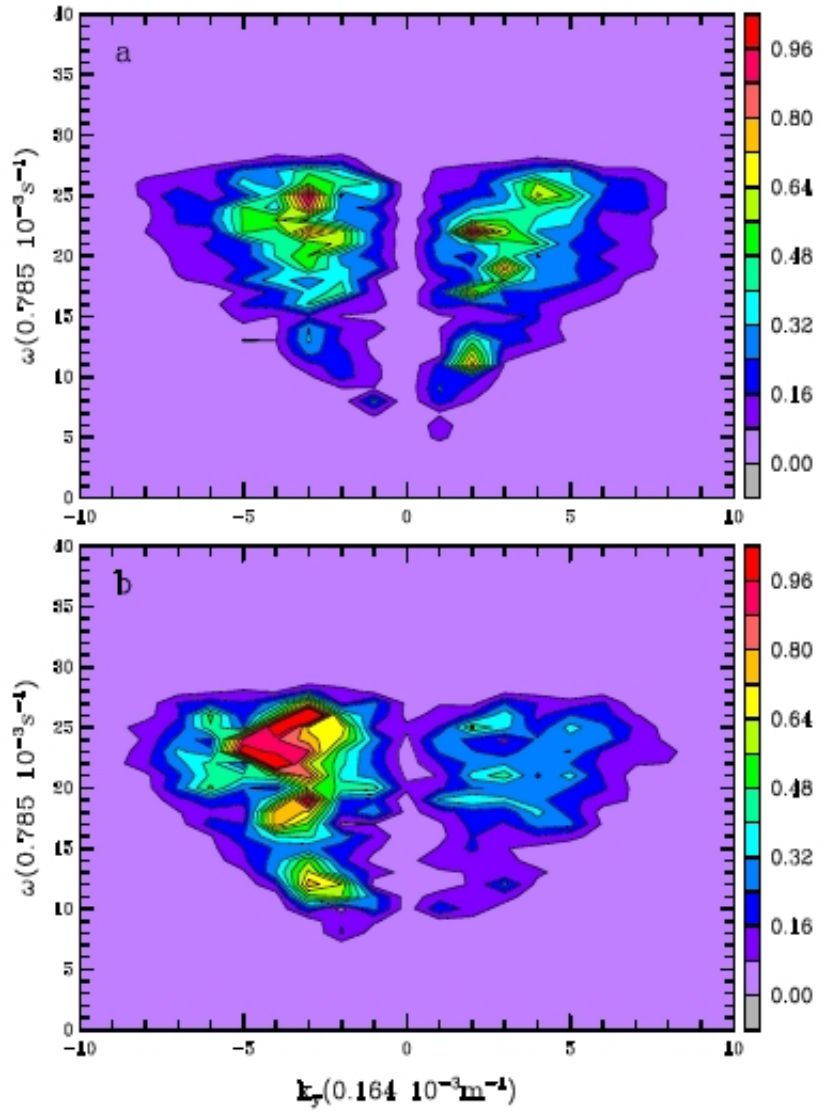


Figure 4: Normalized co-spectra of (V,W), averaged over the streamwise wavenumbers at $z=24$ km without rotation (a), and with rotation (b).

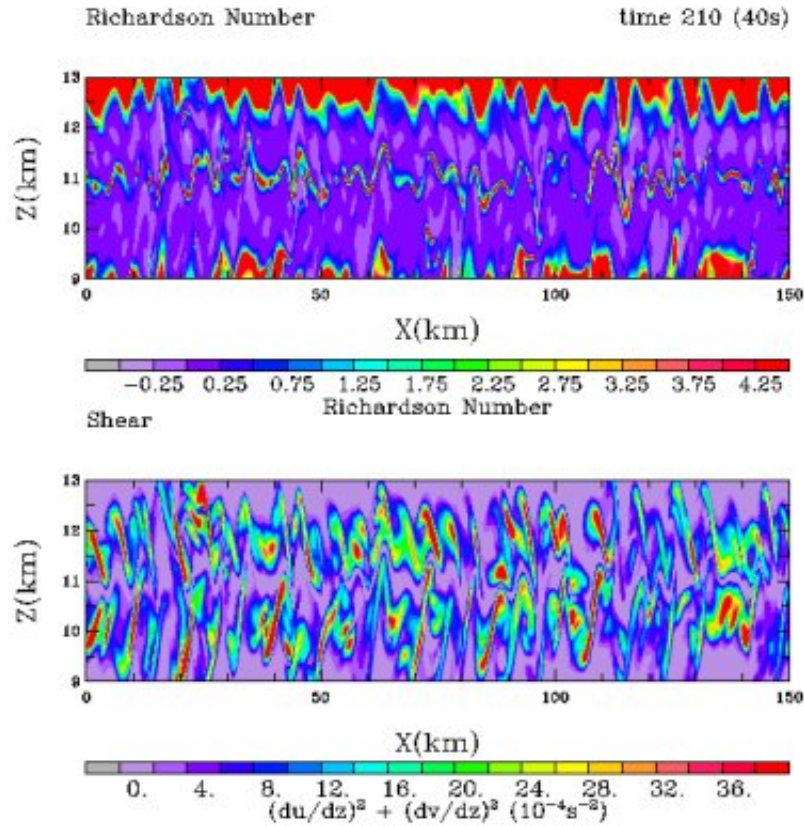


Figure 5: Upper panel: (streamwise-altitude) cross section of the Richardson number in the jet region at $y=70$ km and $t=2.34$ h; lower panel: (streamwise-altitude) cross section of the square of the shear in the jet region at $y=70$ km and $t=2.34$ h

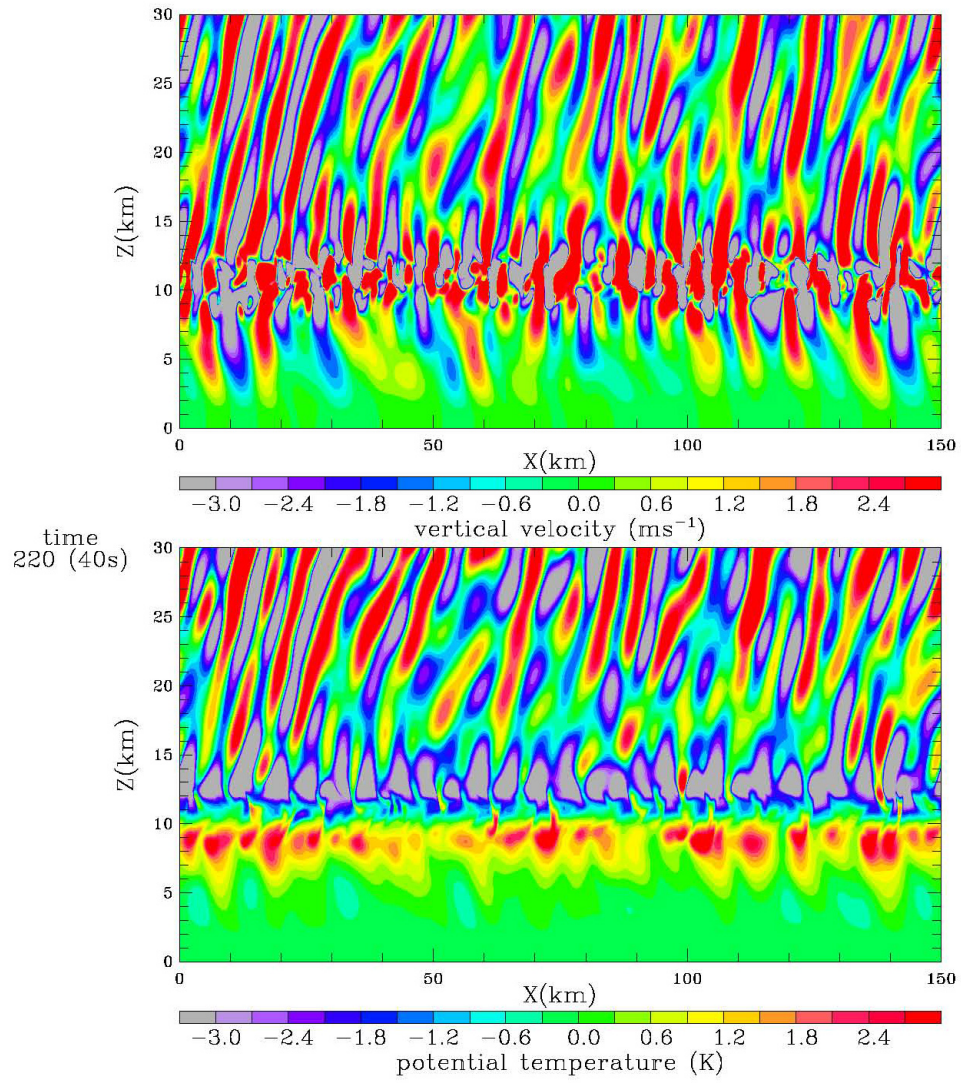


Figure 6: Upper panel: (x-z) cross section of vertical velocity fluctuation; lower panel: (x-z) cross-section of potential temperature (mean + fluctuation). The jet stream is centered at $z=11\text{km}$

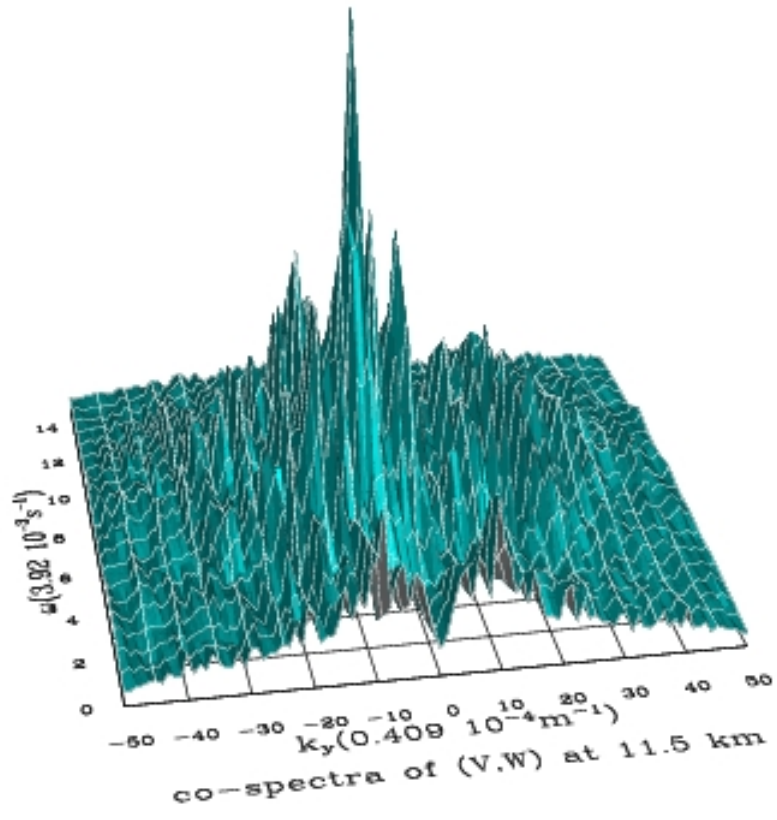


Figure 7: Co-spectra of spanwise velocity and vertical velocity fluctuations on the upper flank of the jet (11.5 km). ω is the frequency and k_y is the spanwise wavenumber. Cospectra are averaged along the streamwise wavenumbers.

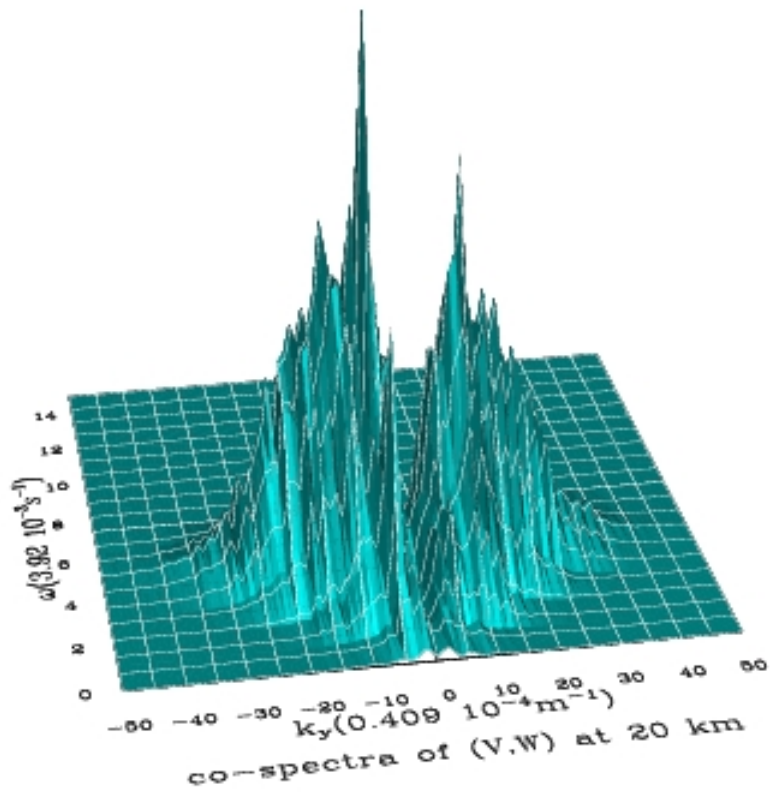


Figure 8: Co-spectra of spanwise velocity and vertical velocity fluctuations in the stratosphere at 20 km. ω is the frequency and k_y is the spanwise wavenumber. Cospectra are averaged along the streamwise wavenumbers.

2 Characterization of Stratospheric Clear Air Turbulence Induced by Helical Shear

The methodology described in Section 1 was applied to the analysis of data from the FASTEX campaign of measurements in the North Atlantic (Fronts and Atlantic Storm-Track EXperiment): mountain waves generated by the Greenland topography were transmitted across a strong polar jet, with observed and measured CAT layers. The numerical code was modified to include splitting of the spanwise background velocity induced by the directional shear. Strong Jet Streams (around 10-12km) impact on the transmission of mountain waves and radiate *polarized* Inertia-Gravity waves into the lower Stratosphere (12-25km). Our 3D code resolved thin stratospheric long lived CAT layers; those are induced by high helical (horizontal directional) shear associated with helical velocity fields of such polarized waves (rapid vertical change of horizontal wind direction within the CAT layer). The propagation of polarized waves into the lower stratosphere is characterized by *collapse of stability inside thin CAT layers*. We discovered mechanisms for genesis of CAT layers in the lower stratosphere from large amplitude waves transmitted through the tropopause and radiated from a broad jet stream in real atmospheric conditions.

The field phase of FASTEX took place in January and February 1997, in the Atlantic Ocean, both near and across Greenland, with waves generated by both the topography (mountain waves) and mesoscale fronts passing through the area (inertia-gravity waves). The strongly deformed jet stream further generated large amplitude radiated inertia-gravity waves into the stratosphere. FASTEX provides a rich data base that includes simultaneous in situ balloon measurements of wind, temperature, pressure, etc. from the ground up to 30 km. This data cover the jet stream region near the tropopause as well as the lower stratosphere, with a vertical resolution that allows to resolve both the jet and the inertia-gravity waves induced by the jet. Many profiles of potential temperature show localized regions in the stratosphere of reduced stability (mixed layers). These layers are closely related to inertia-gravity waves. Figure 9a shows measured vertical profiles of eastward wind and northward wind from a sounding operated during FASTEX on January 2, 1997, at locations straddling both Greenland shore mountains and the Atlantic Ocean. The wind profiles show a jet near the tropopause (10km) that is oriented toward the North (horseshoe dip of the polar jet). High activity of I-G waves is evident in the stratosphere. Notice the adiabatic (near vertical) profiles of potential temperature around $z = 14.5km$ and $z = 17km$: these are mixed CAT layers with localized regions of reduced stability. Thin Stratospheric CAT layers cannot be resolved even by latest generation of Weather Research and Forecasting (WRF) mesoscale codes. We applied our methodology (microscale code) to the resolution of these two observed and measured CAT layers. In particular, mean background potential temperature and mean horizontal winds are from the FASTEX Data Base.

Figure 9b shows the hodograph of the *measured* and filtered horizontal wind, that is the horizontal wind velocity vector rotates clockwise with higher altitude in a "corkscrew" helicoidal motion; this indicates upward propagation of energy. The horizontal wind direction changes very rapidly within the first (14km – 15km) and the second (16.5km – 17.8km)

CAT layer. These layers are created by high helical (directional horizontal) shear associated with the helical horizontal velocity field of the propagating polarized I-G wave. Figure 10 shows a $y - z$ (spanwise-altitude) cross-section of the Richardson number and the similar cross-section of the square of the shear $((du/dz)^2 + (dv/dz)^2)$. The CAT layers at $14.5km$ and $17km$ are characterized by a strong mixing instability, with $R_{ig} \leq 0.25$ and strong shear production. This spanwise cross-sections demonstrate the fully 3D nature of the shear turbulence within the CAT layers. In between the layers, R_{ig} increases considerably and shear collapses. This is confirmed by the mirror $x - z$ (streamwise-altitude) cross-sections of R_{ig} and shear in Figure 11. Figure 12 shows both $x - z$ (streamwise-altitude) and $y - z$ (spanwise-altitude) cross-sections of Brunt-Vaisala frequency. The values of $N^2(z)$ are much lower within the CAT layers than in between layers. Values of Brunt-Vaisala frequency close to zero or slightly negative are consistent with unstable stratification, local convective instabilities and strong mechanical turbulence within the CAT layers. In Figure 13, both $x - z$ (streamwise-altitude) and $y - z$ (spanwise-altitude) cross-sections of vertical velocity fluctuations are given. Local high vertical velocity patches prevail within the CAT layers, with streamwise-spanwise spans of up to $2km$, and few hundred meters in the vertical. Finer resolution shows that vertical velocity can jump from $-10ms^{-1}$ to $+10ms^{-1}$ within few hundred meters in the horizontal; this is the conundrum for the UAVs autopilot, inducing pitch oscillations which can put the platform itself at risk.

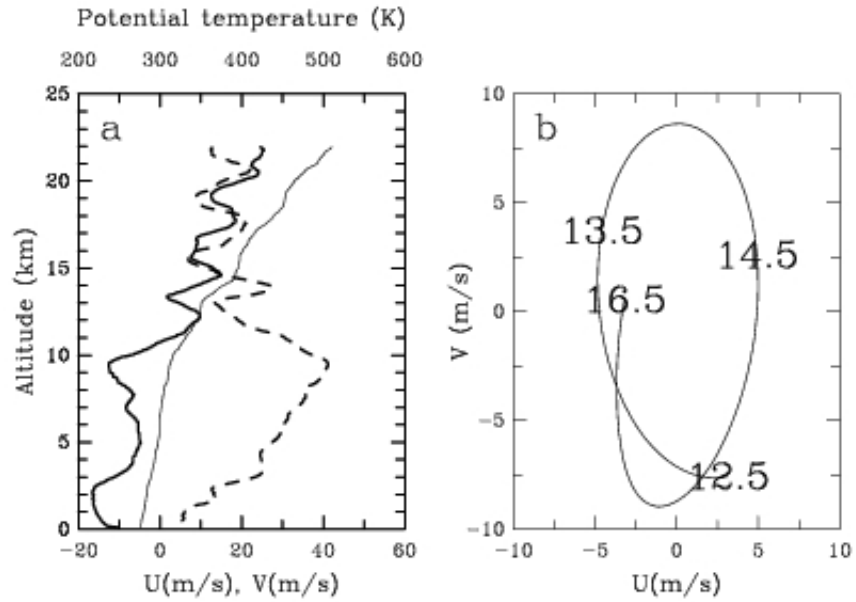


Figure 9: (a) Vertical profiles of eastward (thick solid), northward (dashed) and potential temperature (thin solid) measured by a sounding at (37.65W,65.52N) operated during FASTEX on 2 January 1997 at 6 UTC; (b) hodograph of wind fluctuations. Altitudes are given in *km*

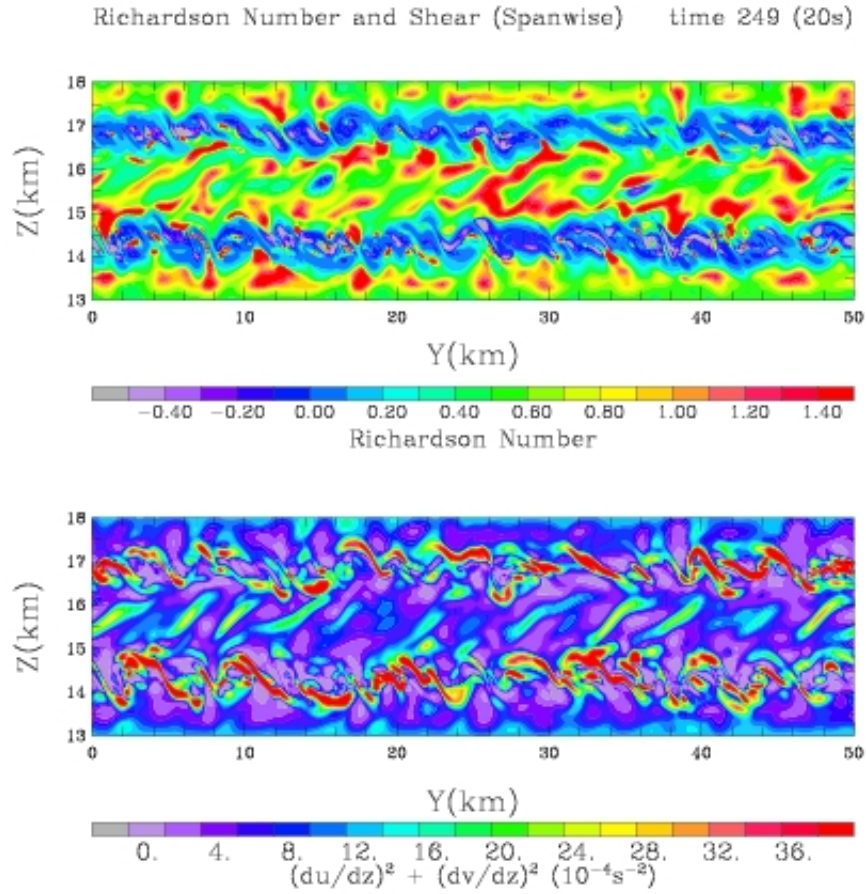


Figure 10: CAT layers; upper panel: (spanwise-altitude) cross section of Richardson number at $x=25$ km and $t=1.39$ h. Lower panel: (spanwise-altitude) cross section of the square of shear at $x=25$ km and $t=1.39$ h.

Richardson Number and Shear (Streamwise) time 249 (20s)

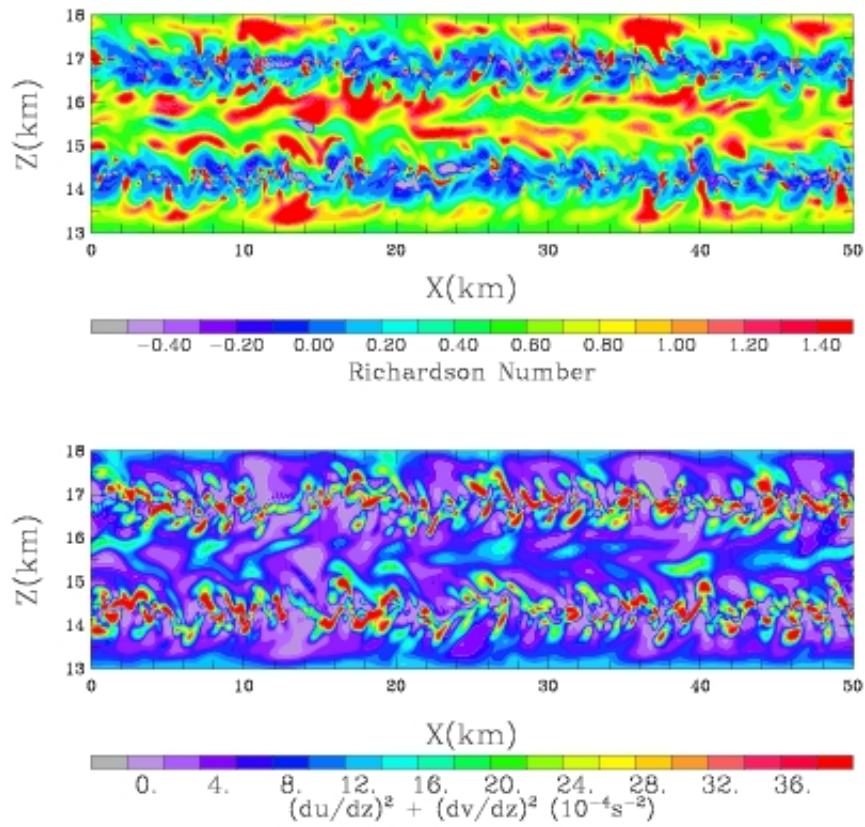


Figure 11: CAT layers; upper panel: (streamwise-altitude) cross section of Richardson number at $y=25$ km and $t=1.39$ h. Lower panel: (streamwise-altitude) cross section of the square of shear at $y=25$ km and $t=1.39$ h.

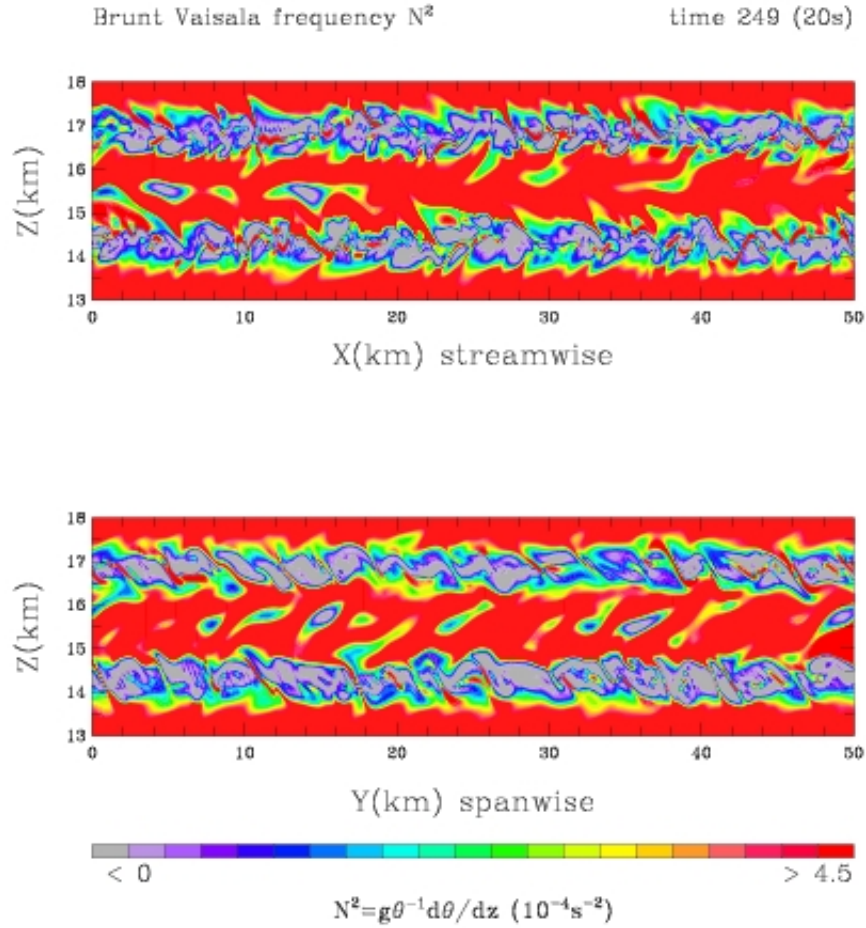


Figure 12: CAT layers; upper panel: (streamwise-altitude) cross section of Brunt Vaisala frequency at $y=25$ km and $t=1.39$ h. Lower panel: (spanwise-altitude) cross section of Brunt Vaisala frequency at $x=25$ km and $t=1.39$ h.

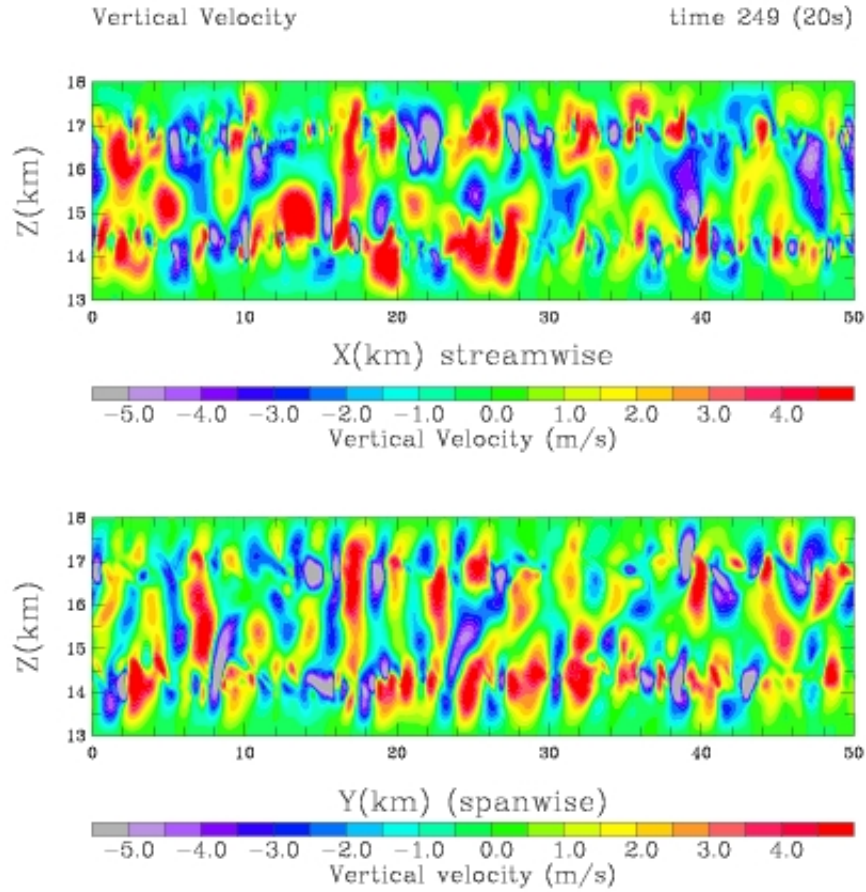


Figure 13: CAT layers; upper panel: (streamwise-altitude) cross section of vertical velocity at $y=25$ km and $t=1.39$ h. Lower panel: (spanwise-altitude) cross section of vertical velocity at $x=25$ km and $t=1.39$ h.

3 Nonhydrostatic fully compressible 3D Navier-Stokes equations for atmospheric dynamics: vertical nesting and adaptive gridding in coupled mesoscale/microscale codes

The 3D Nonhydrostatic, Fully Compressible Navier-Stokes Equations for Atmospheric Dynamics are:

$$\partial_t U + (\nabla \cdot \mathbf{V}u)_\eta + \alpha \partial_x p + (\alpha/\alpha_d) \partial_\eta p \partial_x \phi = F_U \quad (19)$$

$$\partial_t V + (\nabla \cdot \mathbf{V}v)_\eta + \alpha \partial_y p + (\alpha/\alpha_d) \partial_\eta p \partial_y \phi = F_V \quad (20)$$

$$\partial_t W + (\nabla \cdot \mathbf{V}w)_\eta - g[(\alpha/\alpha_d) \partial_\eta p - \mu_d] = F_W \quad (21)$$

$$\partial_t \Theta + (\nabla \cdot \mathbf{V}\theta)_\eta = F_\theta \quad (22)$$

$$\partial_t \mu_d + (\nabla \cdot \mathbf{V})_\eta = 0 \quad (23)$$

$$\partial_t \phi + \mu_d^{-1} [(\mathbf{V} \cdot \nabla \phi)_\eta - gW] = 0 \quad (24)$$

$$\partial_t Q_m + (\nabla \cdot \mathbf{V}q_m)_\eta = F_{Q_m} \quad (25)$$

These equations are cast in conservative form and are formulated using a terrain-following pressure coordinate denoted by η and defined as: $\eta = (p_{dh} - p_{dht})/\mu_d$ where $\mu_d = p_{dhs} - p_{dht}$, and μ_d represents the mass of the dry air in the column and p_{dh} , p_{dht} and p_{dhs} represent the hydrostatic pressure of the dry atmosphere and the hydrostatic pressure at the top and the surface of the dry atmosphere.

In these equations, (u, v, w) are the velocity components, θ is the potential temperature, p is the pressure, g is the acceleration of gravity, $\phi = gz$ is the geopotential. \mathbf{V} and Θ are coupled velocity vector and potential temperature and are given by: $\mathbf{V} = \mu_d \mathbf{v}$, $\mathbf{v}(u, v, w)$, $\Theta = \mu_d \theta$. The right-hand-side terms F_U , F_V , F_W , and F_θ represent forcing terms arising from model physics, turbulent mixing, spherical projections, and the earth's rotation.

The above governing equations are resolved together with the diagnostic equation for coupled dry inverse density

$$\partial_\eta \phi = -\alpha_d \quad (26)$$

and the diagnostic relation for the full pressure (vapor plus dry air) $p = p_0 (R_d \Theta_m / p_0 \alpha_d)^\gamma$. In these equations, α_d is the coupled inverse density of the dry air (μ_d / ρ_d) and α is the coupled inverse density taking into account the full parcel density $\alpha = \alpha_d (1 + q_v + q_c + q_r + q_i + \dots)^{-1}$ where q_* are the mixing ratios (mass per mass of dry air) for water vapor, cloud, rain, ice, etc. Additionally, $\Theta_m = \Theta (1 + (R_v / R_d) q_v) \approx \Theta (1 + 1.61 q_v)$, and $Q_m = \mu_d q_m$; $q_m = q_v, q_c, q_i, \dots$

The pressure gradient terms in the momentum equations have the following forms:

$$\begin{aligned}
 P_x &= (\alpha/\alpha_d)(\alpha'_d\bar{p}_x + \alpha_d p'_x + \bar{\mu}\phi'_x + p'_\eta\phi_x) \\
 P_y &= (\alpha/\alpha_d)(\alpha'_d\bar{p}_y + \alpha_d p'_y + \bar{\mu}\phi'_y + p'_\eta\phi_y) \\
 P_z &= -g((\alpha/\alpha_d)p'_\eta - \mu' + (\alpha/\alpha_d - 1)\bar{\mu})
 \end{aligned}$$

and equation (26) takes the form: $\partial_\eta\phi' = -\alpha'_d$ The prime variables are the deviation from the reference state (i.e. $p' = p - \bar{p}$), and the reference state have to depend on the altitude only, and satisfies the hydrostatic balance for the above formulation to hold.

Non-homogeneous, anisotropic turbulence computations require that a fine mesh be used to encompass all pertinent multiscales of stratospheric mechanical and optical turbulence (Joseph et al, 2004; Mahalov et al, 2006; 2007; Tse et al, 2003). This, coupled with stiff velocity and temperature gradient profiles, presents significant challenges for nesting and adaptive gridding.

Our technical approach is based on microscale vertical nesting and adaptive vertical gridding in coupled mesoscale/microscale codes. Vertical nesting is implemented by coupling the higher resolution mesoscale nest with a sequence of embedded microscale nests, with increased resolution in both the horizontal and vertical, and adaptive vertical gridding to resolve nonlinear processes responsible for the formation of laminated turbulent structures near the tropopause and in the lower stratosphere.

The numerical method uses the time-split integration scheme following the technique developed by Wicker and Skamarock (2002). In this method, low-frequency modes that are meteorologically significant are integrated using a third-order Runge-Kutta time integration scheme; while high-frequency acoustic modes are integrated implicitly in the vertical with smaller time steps to maintain stability. The spatial discretization uses a C grid staggering: normal velocity are staggered one-half grid length from the thermodynamic variables. Advection of vector and scalar fields is in the form of flux divergence, and is performed using the third order Runge-Kutta time-integration scheme, the advection uses a fifth and third order accurate up-winded spatial discretization in the horizontal and the vertical respectively.

Both upper and lateral boundary conditions are nudged within relaxation zones to the finest mesoscale nest fields including the vertical velocity. The vertically nudged upper boundary conditions prevents the formation of spurious wave reflection at the top of the domain (Mahalov et al, 2007). To test the relaxation, numerical simulations were conducted using lateral relaxation for all fields and compared with another simulation where all fields were relaxed except the vertical velocity. The numerical code is written in Fortran90 to facilitate its portability to different platforms. The code is fully parallelized using MPI. The accuracy of the numerical simulation results and the relaxation of the boundary conditions were tested by comparing the model results in idealized moist and dry simulations for which the behavior of the expected solution is known and have been validated by other non-hydrostatic models. This includes mountain wave generation above an idealized topography (Figure 14), and squall-line developments within moist deep convection.

The simulations conducted for these studies were performed on the ASC MSRC SGI Altix "Eagle", NAVO MSRC IBM P5 "Babbage" platform, and HPC Intel Xeon cluster at Arizona State University (ASU).

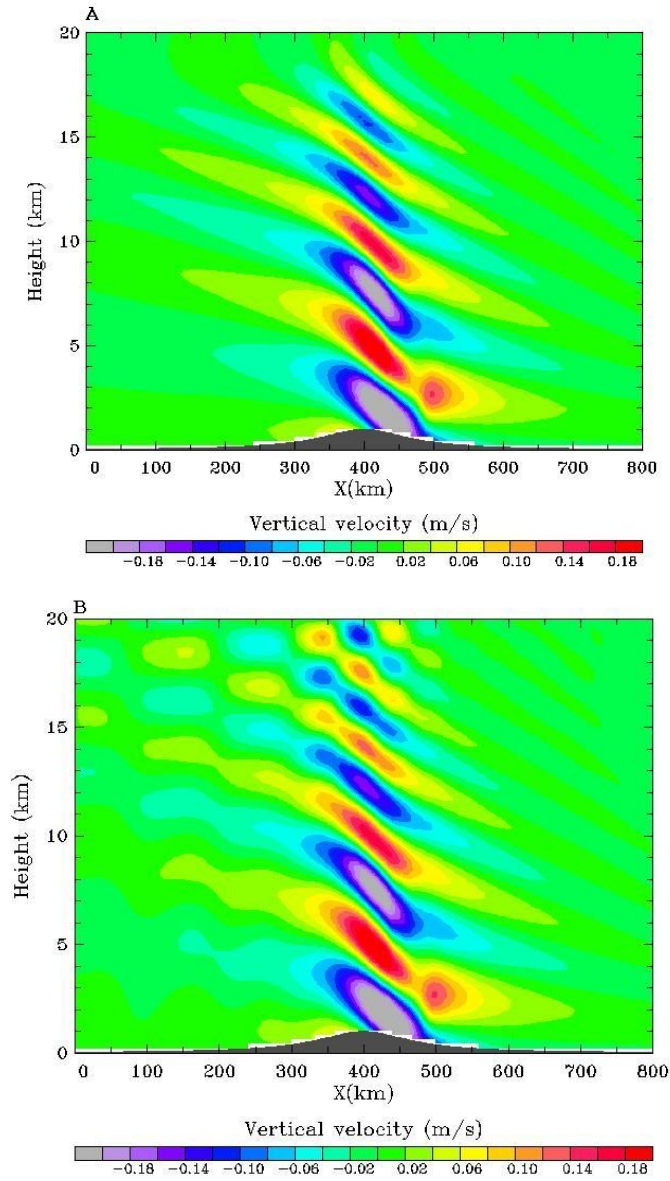


Figure 14: Vertical cross sections of vertical velocity from idealized microscale simulations using (a) vertical relaxation to the background state, and (b) without any vertical relaxation.

4 Multi-scale resolution of laminated structures in the Upper Troposphere/Lower Stratosphere (UTLS) in coupled mesoscale/microscale code simulations

Stratospheric mechanical turbulence (altitudes 10-25km) is characterized by patchy high frequency fluctuations in the stratospheric wind fields and long-lived energetic eddies with a few hundred meters scales in the vertical. The thin Clear Air Turbulence (CAT) layers negatively impact on the effective control, stability and performance of the newest generation of Unmanned Air Vehicles (UAV) such as the Global Hawk. Flying through stratospheric CAT causes the autopilot to begin pitch oscillations that seriously degrade photographic and synthetic aperture radar performance as well as put the platform itself at risk. While there is a need for real time forecast of these thin stratospheric CAT layers, these cannot be resolved by even the latest generation of Weather Research and Forecasting (WRF) mesoscale meteorological codes. Our goal is to enable forecasting of non-linear, non-monochromatic inertia-gravity waves with large horizontal wavelengths (few hundred kilometers) which generate thin (few hundred meters) CAT layers. Coupled tropospheric/stratospheric forecasting CAT and Optical Turbulence (OT) layers is a challenge for real time operational forecasting.

High resolution coupled mesoscale/microscale code simulations were carried out to predict and characterize stratospheric CAT and OT layers and to examine and parameterize wind-shear and gravity waves evolution under representative mesoscale atmospheric conditions (jetstreams, topography), their respective modes of instability, morphology and dynamics, and subsequent breakdown into turbulent motion. This information in turn is used to improve prognostic parameterizations of eddy-mixing coefficients and diagnostic parameterizations of mechanical and optical turbulence for the tropopause and lower stratosphere regions.

The Terrain induced Rotor Experiment (TREX) campaign represents an important case of turbulent dynamics associated with topographic gravity waves. During this campaign, several radiosondes were launched from the upwind side of Owens Valley, CA. Vertical Profiles of temperature and wind components were measured with high vertical resolution from the ground up to 30km. Many profiles exhibit high temperature and wind wave-like fluctuations in the lower stratosphere, with different vertical wavelengths and localized adiabatic layers where potential temperature gradients are small.

Figure 15 (left panel) shows vertical profiles of potential temperature, eastward and northward wind components, from measurements during TREX performed by a balloon launched at (36.49 N, 118.84 W) on April 1, 2006 at 7:50 UTC. High activity of mountain waves is evident from these profiles. The potential temperature profile shows many regions above the tropopause (11km) where the vertical gradients are small (i.e. 12km, 14km and 20km). The vertical profile of the square of Brunt Vaisala frequency (Figure 15 right panel) calculated from the potential temperature shows strong inhomogeneities. At the tropopause, we

notice a strong increase in stability around 11.2km with values reaching $N^2 = 19 \times 10^{-4} s^{-2}$ and exceeding those usually observed in the stratosphere ($N^2 = 4 \times 10^{-4} s^{-2}$). Above this level, the stability decreases within thin adiabatic layers in the lower stratosphere; and increases again thereafter and reaches a second maximum just below 13km. This laminated structure with layering of local maxima and minima in stability was also observed in other profiles performed during TREX campaign. The structure of these profiles indicates high activity of mountains waves, with complex dynamics involving multiscale processes as indicated in the profiles presented in Figure 15 that show coexistence of smaller and larger vertical wavelengths. Real case simulations with resolutions that are higher than those used in standard mesoscale codes are required to adequately predict and understand these process. These simulations also show that regions near the tropopause and in the lower stratosphere experience wave breaking events induced by localized convective and shear instabilities. The resulting inhomogeneous changes in stability within short distances have in turn dramatic impacts on mountain wave propagation itself.

Our simulations with embedded microscale nests demonstrated the deep change of nature of these mountain waves when transmitted through the tropopause (around 11-12km). Strong CAT layers are associated with stiff adiabatic layers of potential temperature. These layers have complex streamwise-spanwise structures, are located as low as 13.5km up to 20km and higher in the stratosphere. In between these adiabatic potential temperature layers, we evidenced and fully resolve strong countergradient layers of convective instabilities, with locally unstable stratification. This intricate turbulent coexistence of thin alternating layers of sharp positive/negative gradients of potential temperature was not expected nor resolved by previous simulations in the literature, albeit diagnosed in TREX high altitude measurements. The feedback of stiff temperature layers onto highly turbulent patches of vertical velocity presents a challenge to the control of UAV's and other high altitude platforms.

The innermost microscale nest simulations used initial and boundary condition from the finest mesoscale nest. Both upper and lateral boundary conditions were relaxed towards the finest WRF nest fields. Figure 16 shows topography for the innermost microscale nest and the wind vector field at 12 km altitude simulated by the microscale nest on April 1, 2006 at 8:00 UTC. The wind directions are dominated by south-westerlies in agreement with observations. This is a validation of our microscale code. We notice that the relaxation of the wind field is very smooth at the boundaries achieved through implementation of relaxation and nudging techniques in our code. Also, regions with strong turbulent flow were found above the valley, towards the south of the balloon trajectory. In these regions the horizontal wind shows strong drag, and the direction of the wind is complex. This turbulent flow is more evident in Figure 17. This figure shows longitude (118.56 W, 117.42 W)-altitude cross-section at latitude 36.82 N for potential temperature (contour) and vertical velocity (color) on April 1, 2006 at 8:00 UTC for the innermost microscale domain. The potential temperature shows multi-scales patterns with fine structures that are not resolved by the mesoscale finest nest. Near the tropopause (12km) a localized layer is found where the potential temperature contours are well packed together indicating strong local increase in stability. This layer shows a wave-like pattern with horizontal wavelengths as

short as $\approx 6km$ near $x = 40km$. This wave cannot be directly excited by topography, since its wavelength is much smaller than the horizontal scale of the mountains, and is not observed in potential temperature below 12 km at upper tropospheric levels (9-10km). This evidence that the wave observed in the high stratification layer is generated locally by nonlinear interactions and/or wave breaking. At some levels above 12 km, there are regions in the lower stratosphere where stratification decreases within adiabatic layers, while other regions show localized stiff gradients. These strong local variations in stability and local shear together with dipoles of high vertical velocity patches are evident in a zoom of these fields in the UTLS region (figure 18). The resulting strong local inhomogeneities in stratification with layering of local maxima and minima are observed during TREX (Figure 15) and have in turn dramatic impacts on wave propagation. High stratification tends to shorten the vertical wavelength of a propagating wave and tends to increase its horizontal wind amplitude resulting in local unstable regions with high local shear; while adiabatic and convectively unstable layers may develop regions where waves are trapped or even reflected. This complex nonlinear dynamics involving multiscale interactions result in a turbulent flows in the lower stratosphere as depicted in Figure 17, where the wavelength of the topographic wave causing this dynamics is hardly identified (the dominant wavelength of the topographic wave should match the horizontal scale of the mountain).

Figures 19 and 20 show longitude(118.56W, 117.42W)-altitude cross-sections from the innermost microscale nest at latitude 36.82N for Richardson number and the shear field respectively. Patches of low Richardson number are well resolved and are found primarily near the ground and at upper levels around the tropopause and in the lower stratosphere in the UTLS region. We notice that small scales develop in potential temperature primarily in these regions (Figure 17). These strongly mixed turbulent layers are induced by nonlinear interactions triggered by nonlinear rotor waves near the ground and by wave breaking and wave refraction around the tropopause.

We investigated how mountain waves induced by topography propagate through the tropopause and result in formation of several sharp adiabatic layers with spatial scales smaller than the wavelength of topographic waves. Below adiabatic layers at the tropopause level there are regions of high stability characterized by large vertical gradients of potential temperature. This has been observed in several radiosonde profiles during the TREX campaign of measurements. These regions of inhomogeneous gradients can further impact the propagation and transmission of upward propagating topographic waves. These are strongly 3D nonlinear phenomena.

Accomplishments/Breakthroughs

- Microscale vertical nestings resolve thin adiabatic layers of potential temperature and fine stratospheric CAT patches of vertical velocity in real atmospheric conditions. Improved predictability of mechanical turbulence (patches of strong vertical velocity) and optical turbulence (peaks of Cn2 at turbulent interfaces of adiabatic layers).
- Contour levels of potential temperature show high activity of refracted mountain

waves with nonlinear changes of amplitudes and phases; significant wavelength shortening of refracted waves above 10km: increased/decreased regions of stability and coupling with strong mean flow variability.

- Effective resolution of intense wave breaking events above the tropopause resulting in formation of several sharp adiabatic layers. Below adiabatic layers at the tropopause level there are regions of high stability characterized by large vertical gradients of potential temperature. This was observed in several radiosonde profiles during the TREX campaign of measurements.
- Laminated structure and layering in the vertical profiles of N^2 near the tropopause and in the lower stratosphere observed in the TREX campaign of measurements is fully resolved by the microscale nests.

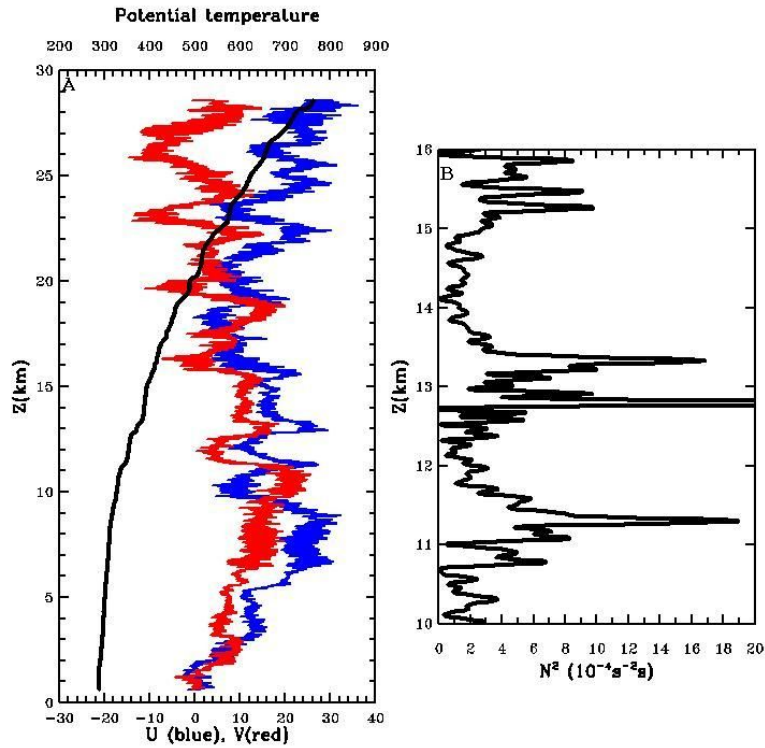


Figure 15: (a) Potential temperature (black), eastward wind (blue), and northward wind (red) from balloon measurements during T-REX. The balloon was launched at (36.49 N, 118.84 W) on April 1, 2006 at 7:50 UTC. (b) vertical profile of Brunt Vaisala frequency in the UTLS region showing strongly laminated structures.

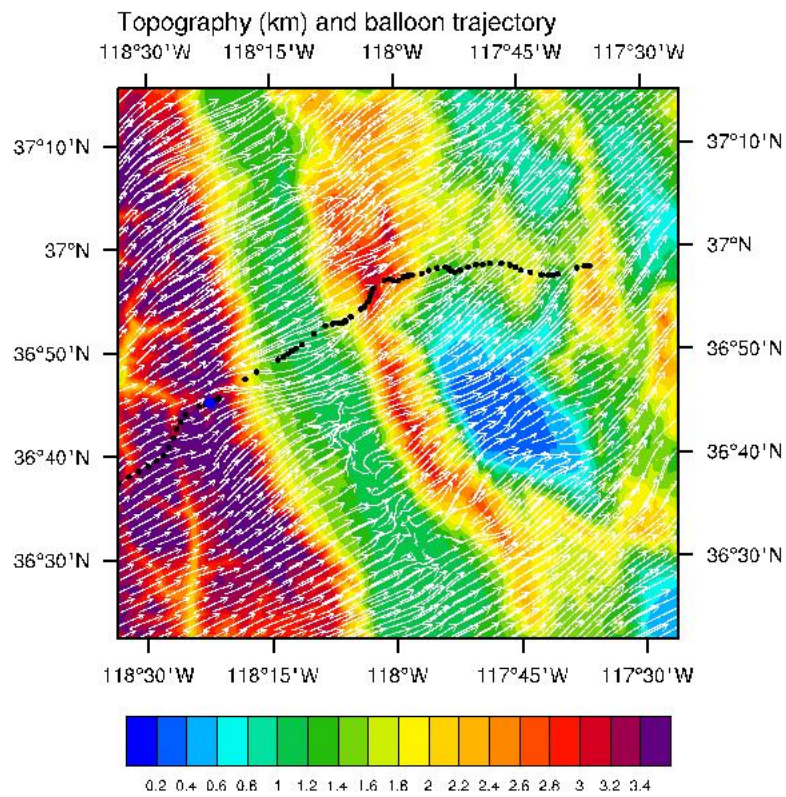


Figure 16: Wind vector fields at 12 km and topography used for the microscale nest. The black curve shows the balloon trajectory.

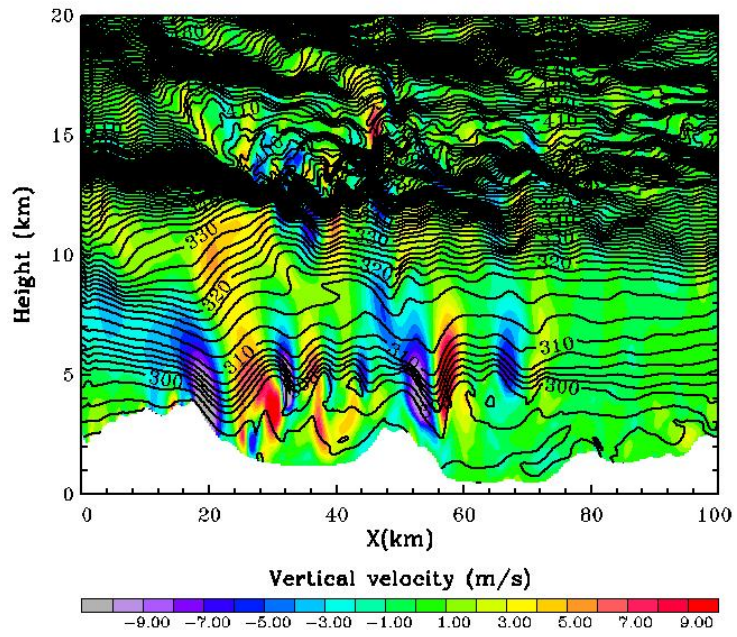


Figure 17: Longitude-altitude cross-sections for potential temperature (contour) and vertical velocity (color) from the microscale nest. The time is 8:00 UTC, April 1, 2006.

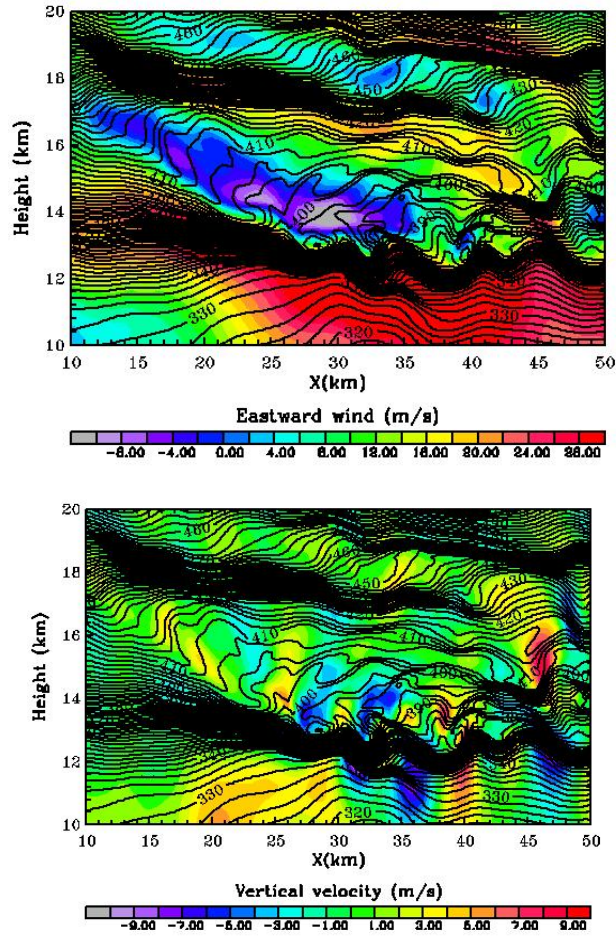


Figure 18: Longitude-altitude cross-sections for: (upper panel) potential temperature (contour) and eastward wind (color); and (lower panel), potential temperature (contour) and vertical velocity from the microscale nest. The time is 8:00 UTC, April 1, 2006.

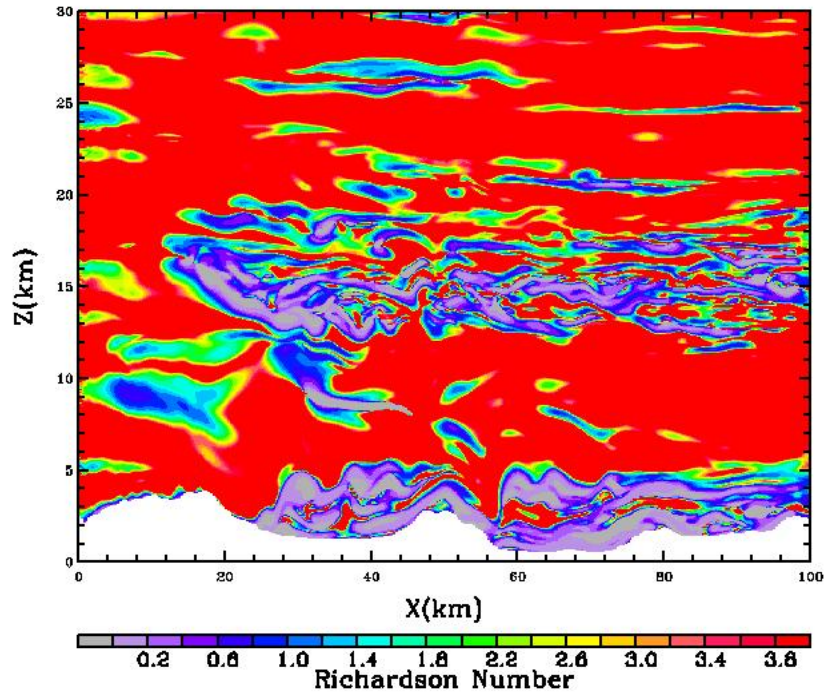


Figure 19: Longitude-altitude cross-sections for Richardson number from the microscale nest. The time is 8:00 UTC, April 1, 2006.

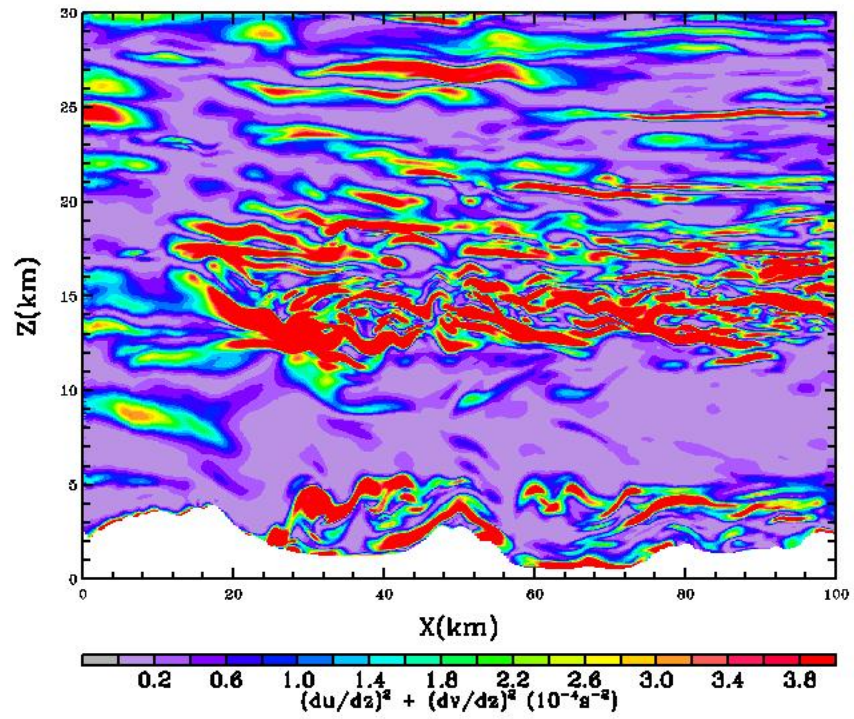


Figure 20: Longitude-altitude cross-sections for the square of the shear from the microscale nest. The time is 8:00 UTC, April 1, 2006.

5 Multi-scale resolution and forecasting of stratospheric Optical Turbulence (OT) layers

High Resolution microscale code simulations were performed to predict and characterize stratospheric Optical Turbulence (OT) layers induced by jet streams and gravity waves under various local atmospheric conditions during the Hawaii 2002 campaign. We obtained local distributions of simulated optical turbulence (C_n^2) in the upper troposphere/lower stratosphere using explicit simulations that show strongly laminated structures with thin layers of high values of refractive index. These layers are characterized by steep vertical gradients of potential temperature and are located at the edges of relatively well mixed regions produced by shear instabilities induced by jet stream and polarized inertia-gravity waves.

Figure 21 shows vertical profiles of eastward and northward winds, and potential temperature from a sounding obtained at Hawaii (155.3 W, 19.5 N) on 12 December 2002 at 5 UTC. The wind structure indicates a strong eastward jet with wind maximum in the upper troposphere around 12km. Above the tropopause the winds components exhibit a wave pattern with short vertical wavelength of about 2km. Figure 22b shows the vertical profiles of refractive index coefficient C_n^2 measured simultaneously with the profiles presented in Figure 21. Several peaks are found around 13km and in the lower stratosphere between 15km and 16km. The upper tropospheric peak is located at relatively high shear region at the upper flank of the jet. The peak observed in the lower stratosphere is found well above the upper flank of the jet in a region dominated by short waves. The local hodograph of the wind components (Figure 23a) shows that these waves are long period polarized inertia-gravity waves. The hodograph rotates clockwise with altitude indicating that these waves are carrying energy upwards. The angle of the horizontal wind vector changes with the vertical inducing a directional shear (Figure 23b). This change is not uniform, and it is modulated by a shorter wave with a wavelength that is smaller than 1 km. This shows the presence of polychromatic waves that induce rapid change of horizontal wind direction within short vertical distance. The high helical shear coupled with reduced stability associated with helical velocity and temperature fields of such polychromatic polarized waves result in favorable conditions for developments of shear instabilities that are different from those generated by jet or parallel flows. The instabilities induced by helical shear are three dimensional even at earlier stages of their development, and they are more efficient in developing turbulent and mixing layers. In non-Kolmogorov turbulent environment induced by polarized inertia-gravity waves, fluctuations of temperature and vertical velocity are strongly coupled. Variances of temperature and vertical velocity are modulated by inertia-gravity waves with the corresponding local peaks shifted in space and time. The distributions of these lagged peaks in space and time (maximum values of temperature/vertical velocity variances) are controlled by the polarization of inertia-gravity waves.

Figure 24 shows streamwise and spanwise vertical cross-sections of potential temperature fluctuations from very high resolution simulations initialized with the vertical profiles from measurements over Hawaii's Big Island at (155.3 W, 19.5 N). This simulation used

$1000^2 \times 2000$ grid points with adaptive time stepping and vertical resolution that reaches 1 m. Two layers of high potential temperature fluctuations are found at the upper flank of the jet (13 km) and in the lower stratosphere (16 km) respectively where a helical shear is present. It should be noted that these two types of instabilities different in nature and are very difficult to simulate simultaneously because they evolve with different time and space scales, and to our knowledge have not been resolved in the past. Our simulations required adaptive gridding and time stepping. Potential temperature fluctuations in both layers show well developed turbulent flow that is strongly three dimensional. The structures in the upper layer associated with the helical shear exhibit horizontal scales that are smaller than those in the lower level layer indicating more turbulent flow and efficient mixing. The instability associated with the jet is streamwise and is two dimensional during the growing stage, while the helical instability develops 3D structures immediately, and the growth rate is higher. Above and below these layers we note the presence of structures with larger spatial scales, that are induced by internal waves radiated by these layers. The turbulence associated with these layers is non-Kolmogorov, highly anisotropic and strongly affected by the inhomogeneous stratification.

Figure 25 shows the refractive index coefficient (C_n^2) calculated explicitly from the temperature field shown in the previous figure. Patches of high values of C_n^2 are found around 13 km and 16 km. The location and the values of C_n^2 are in agreement with those found in the observations (Figure 22a, b). We note that simulation of observed values of C_n^2 is a significant challenge for mesoscale codes; and all mesoscale codes failed to predict correct values for the refractive index coefficient. At the interface between the highly turbulent layer below 16km and the non turbulent region above, there are pockets of C_n^2 that are associated with radiated internal waves and entrainment processes at the fluctuating interface. In contrast to well mixed regions, continuous fluctuating interfaces form resulting in amplification of potential temperature gradients and formation of counter gradient flows. The turbulence that develops in these thin interfacial layers where peaks of C_n^2 develop is inhomogeneous, anisotropic and non-Kolmogorov, and is different from the turbulence that form in well mixed regions, which has Kolmogorov statistics. The theories developed for parametrization of optical turbulence and eddy mixing coefficients based on down gradient flows and well mixed regions are therefore not applicable. The conventional Kolmogorov turbulence assumption of constant turbulent Prandtl number (0.7 - 1) does not hold for such flows. Figure 26 shows the vertical profile of the turbulent Prandtl number obtained from our high resolution simulations. It shows a laminated structure with localized peaks around 13 km and 16 km where large peaks and fluctuations of C_n^2 are found (Figure 22). Strong vertical variability of the turbulent Prandtl number is associated with strongly inhomogeneous shear stratified turbulence that characterizes vertical levels of turbulent interfaces located in the upper troposphere and in the lower stratosphere. This strong variability of the turbulent Prandtl is the key mechanism in our sub-grid scale parametrization of non homogeneous shear stratified stratospheric turbulence.

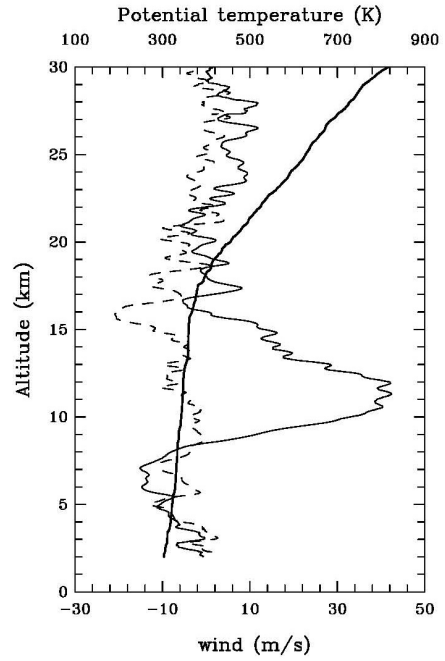


Figure 21: Vertical profiles of eastward wind (thin solid), northward wind (dashed), and potential temperature (thick solid) from a sounding at Hawaii (155.3 W, 19.5 N) on 12 December 2002 at 5 UTC.

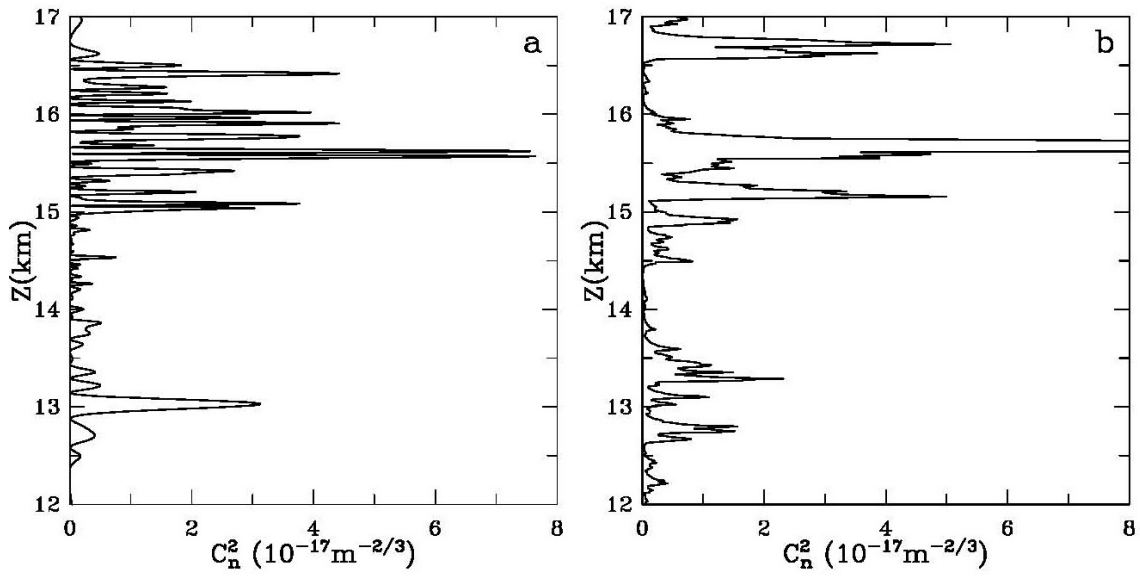


Figure 22: Vertical profile of the refractive index structure coefficient (C_n^2) from (a) numerical simulations; and (b) from observations obtained by a sounding at Hawaii (155.3 W, 19.5 N) on 12 December 2002 at 5 UTC.

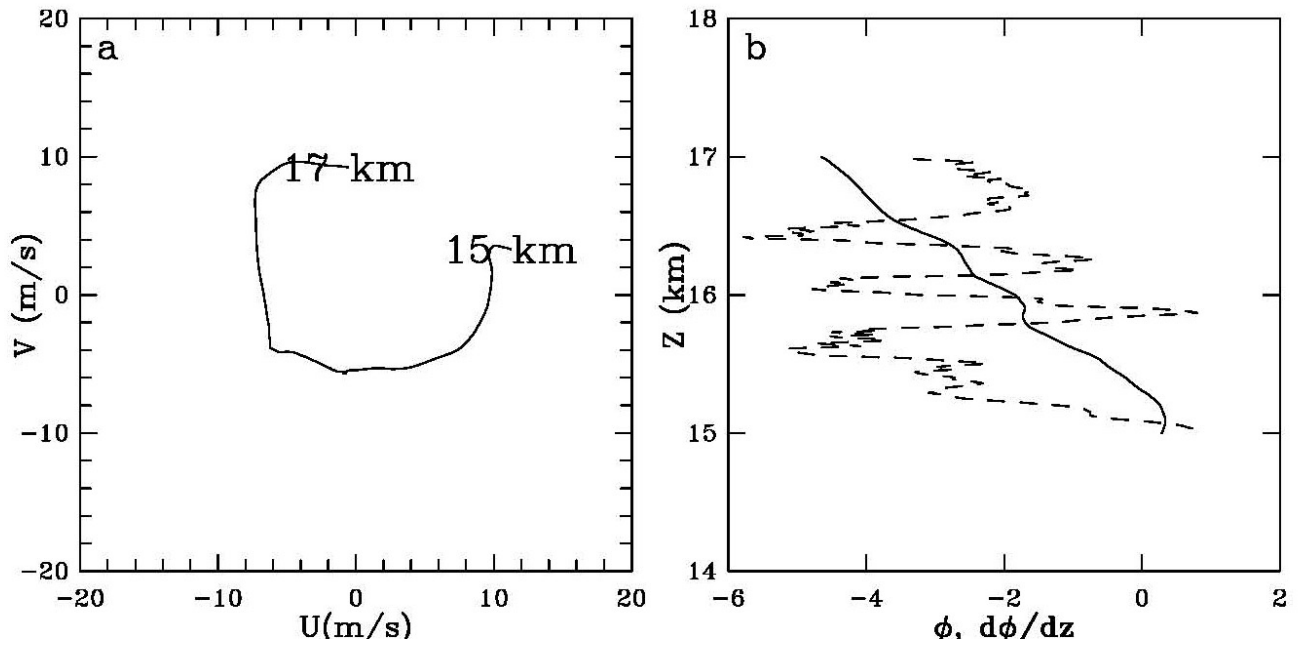


Figure 23: (a) hodograph of the horizontal wind near the tropopause and (b): angle (u,v) (solid) and the variation of the angle with altitude (dashed). The profiles are calculated from the observations shown in Fig. 21.

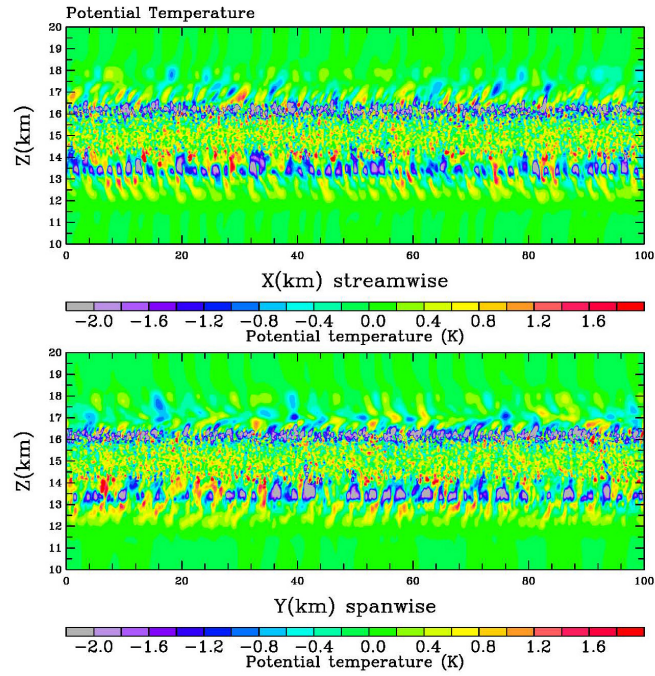


Figure 24: (a) Streamwise-altitude and (b) spanwise-altitude cross-sections for potential temperature from high resolution simulations.

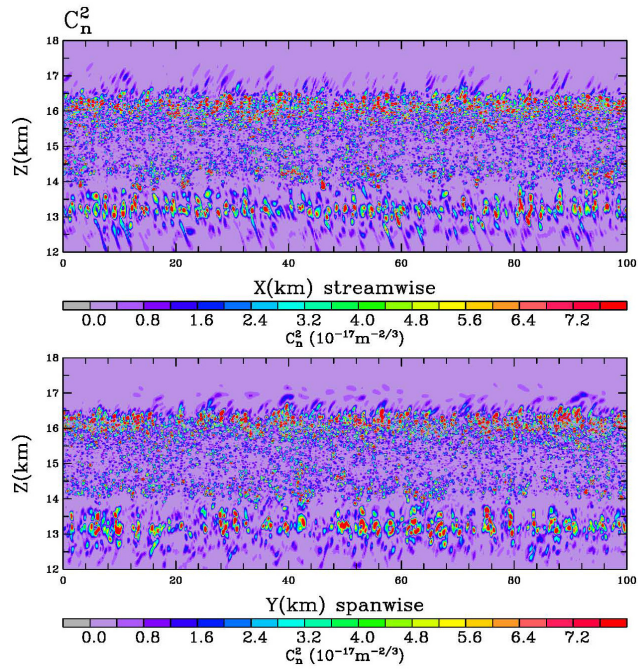


Figure 25: (a) Streamwise-altitude and (b) spanwise-altitude cross-sections for C_n^2 from high resolution simulations.

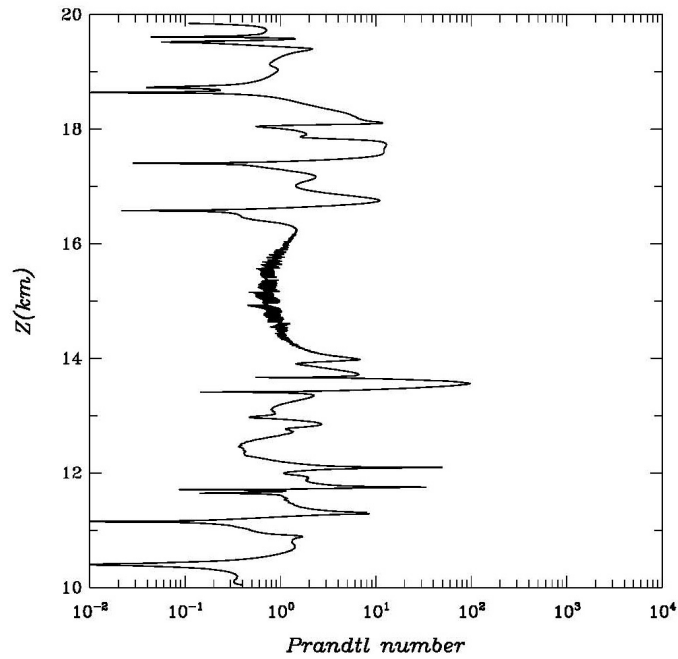


Figure 26: Vertical profile of turbulent Prandtl number from 10km to 20km altitudes over Hawaii's Big Island (155.3 W, 19.5N) on 12 December 2002. Non-Kolmogorov, layered, inhomogeneous shear-stratified turbulence in the upper troposphere/lower stratosphere is characterized by strong vertical variability of the turbulent Prandtl number.

4 Collaboration with Air Force Laboratories

We have closely interacted with the Atmospheric Characterization Airborne Laser (ABL) Program Office managed by Lt Col S. Cocks and Dr. R. Lefevre (ABL/SPO, Kirtland AFB) and with staff at the AFRL/VSBL, Hanscom AFB. This includes Dr. Bob Beland, Dr. Owen Cote, Dr. George Jumper, Dr. Frank Ruggiero and Lt. Col. John Roadcap, AFRL/VSBL.

We have performed high resolution coupled mesoscale (coarse grid input)-microscale (fine vertical gridding) simulations of field measurement campaigns by the Air Force; specifically the series of atmospheric measurements done at the Vandenberg AFB, CA in April-June 2007. Our large scale computations are sponsored by a DoD HPCMPO Challenge Grant ‘Characterization and Prediction of Stratospheric Turbulence for DoD Reconnaissance and Directed Energy Platforms’; co-investigators include Dr. Frank Ruggiero (AFRL/VSBL) and Dr. Joseph Werne (Northwest Research Associates, CO). We have made several presentations at AFOSR/AFRL and DoD HPCMPO workshops and conferences.

We organized and hosted an AFOSR WORKSHOP ‘Challenges of Multiscale Atmospheric Turbulence: High Performance Computing, Physical Modeling and Observational Advances’ at Arizona State University, December 14-16, 2006. More information is on the workshop website <http://hpc.asu.edu/afosrworkshop/>

5 Personnel Supported

- Prof. Alex Mahalov, Department of Mathematics and Statistics, Department of Mechanical and Aerospace Engineering, Arizona State University
- Prof. Basil Nicolaenko, Department of Mathematics, Arizona State University
- Dr. M. Moustouai, Research Scientist, Arizona State University
- Dr. J.J. Liu, Research Scientist, Arizona State University
- Dr. P. Hyde, Research Scientist, Arizona State University
- Dr. W. Carter, Research Scientist, Arizona State University
- Mr. Stephen Eikenberry (student)

6 Selected Publications

1. A. Mahalov, M. Moustouai and B. Nicolaenko (2007), Computational Studies of Inertia-Gravity Waves Radiated from Upper Tropospheric Jets, *Theor. and Comp. Fluid Dynamics*, **21**, No. 6, p. 399-422.
2. JCR Hunt, A. Mahalov, J.R. Pacheco and HJS Fernando (2005), Effects of Rotation and Sloping Terrain on Fronts of Density Currents, *Journal of Fluid Mechanics*, **537**, p. 285-315, 2005.

3. A. Mahalov (2008), Ensemble forecasting of high-impact stratospheric optical turbulence, In ‘Atmospheric Propagation of Electromagnetic Waves’, Proc. of SPIE, IEEE Publications, in press.
4. Y. Giga, A. Mahalov and T. Yoneda (2007), On time analyticity of the Navier-Stokes equations in a rotating frame with spatially almost periodic data, *Physica D*, in press.
5. A. Mahalov, B. Nicolaenko and T. Shilkin (2007), Local Smoothness of Weak Solutions to the Magnetohydrodynamics Equations via Blowup Methods, *Equations aux Derivees Partielles*, **7640**, p. 21.1-21.19.
6. Y. Giga, K. Inui, A. Mahalov and J. Saal (2007), Global Solvability of the Navier-Stokes Equations in Spaces Based on Sum-Closed Frequency Sets, *Advances in Differential Equations*, **12**, No. 7, p. 721-736.
7. F. Golse, A. Mahalov and B. Nicolaenko (2007), Instabilities and Bursting Dynamics of the 3D Euler Equations, *Instability in Models Connected with Fluid Flows*. International Mathematical Series, Edited by C. Bardos and A. Fursikov, Springer.
8. E. Gorshkova, A. Mahalov, P. Neittaanmaki and S. Repin (2007), A posteriori error estimates for viscous flow problems with rotation, *J. Math. Sci.*, **142**, No. 1, p. 1749-1762.
9. A. Mahalov, M. Moustououi and B. Nicolaenko (2007), Multi-Scale Predictability of High-Impact Stratospheric Clear Air Turbulence Events, *IEEE Proceedings of the High Performance Computing Modernization Program Conference*, p. 57-63.
10. Y. Giga, K. Inui, A. Mahalov and J. Saal (2007), Rotating Navier-Stokes Equations in \mathbb{R}_+^3 with Initial Data Nondecreasing at Infinity: The Ekman Boundary Layer Problem, *Arch. for Rational Mech. and Analysis*, **186**, No. 2, p. 177-224.
11. Y. Giga, A. Mahalov and B. Nicolaenko (2007), The Cauchy Problem for the Navier-Stokes Equations with Spatially Almost Periodic Initial Data, *Annals of Mathematics Studies*, **163**, p. 213-223. Special Issue on Mathematical Aspects of Nonlinear Dispersive PDEs (J. Bourgain, C. Kenig and S. Klainerman, eds.), Princeton University Press.
12. Y. Giga, A. Mahalov and S. Matsui (2006), Navier-Stokes Equations in a Rotating Frame with Initial Data Nondecreasing at Infinity, *Hokkaido Mathematical Journal*, **35**, No. 2, p. 321-364.
13. A. Mahalov, B. Nicolaenko and T. Shilkin (2006), $L_{3,\infty}$ Solutions to the Magnetohydrodynamics Equations, *Boundary-Value Problems of Mathematical Physics and Related Problems of Function Theory*, **37**, p. 112-133.
14. Y. Giga, K. Inui and A. Mahalov (2005), Uniform Local Solvability for the Navier-Stokes Equations with the Coriolis Force, *Methods and Applications of Analysis*, **12**, No. 4, p. 381-394.

15. A. Mahalov, B. Nicolaenko and G. Seregin (2007), New Sufficient Conditions of Local Regularity for Solutions to the Navier-Stokes Equations, *J. of Mathematical Fluid Mech.*, Vol. 10, N 1, p. 106-125.
16. A. Mahalov and B. Nicolaenko (2005), High Resolution Numerical Simulations and Modeling of Optical Turbulence across Jet Streams, IEEE Proceedings of the International Society for Optical Engineering Conference 'Atmospheric Optical Modeling, Measurement, and Simulation', **5891**, p. 1081-1089, IEEE Society publications.
17. A. Mahalov and B. Nicolaenko (2006), Characterization of Stratospheric Clear Air Turbulence for Air Force Platforms, IEEE Proceedings of DoD High Performance Computing Modernization Program Conference, IEEE Computer Society Publications, p. 288-295.

7 Selected Plenary Talks and Invited Presentations

The Theory of Highly Oscillatory Problems, Isaac Newton Institute for Mathematical Sciences, Cambridge, UK, 26 March to 30 March 2007, Plenary Talk. Recorded Webcast is on the website

<http://www.newton.cam.ac.uk/webseminars/pg+ws/2007/hop/hopw02/0327/mahalov/>

High Performance Computing Modernization Program (HPCMP) Annual Meeting, Pittsburgh, June 18-21, 2007.

International Conference dedicated to 300th Birthday of Leonard Euler "Mathematical Hydrodynamics: Euler Equations and Related Topics", June 7-9, 2007.

6th International Congress on Industrial and Applied Mathematics (ICIAM07), Mini-Symposium on Navier-Stokes Equations and Related Topics, 16-20 July, 2007, Zurich.

Lighthill Institute of Mathematical Sciences (LIMS) Workshop on Applied Mathematics in Defense Applications, London, May 31-June 1, 2007.

International Conference on "Rotating Fluids in Geophysics", Bernoulli Mathematical Institute, EPFL Lausanne, September 19-22, 2006.

Kyoto Conference on the Navier-Stokes Equations and their Applications, Research Institute for Mathematical Sciences, Kyoto University, Japan, January 6-10, 2006.

International Conference on "Chaos and Disorder in Mathematics and Physics" dedicated to 70th Birthday of Prof. Sinai, Bressanone, Italy, September 18-24, 2005.

International Society for Optical Engineering Conference on Atmospheric Optical Modeling, Measurement and Simulation, San Diego, August 2-3, 2005.

EQUADIFF 11 International Conference on Differential Equations, Comenius University, Bratislava, Slovakia, July 25-29, 2005.

DoD High Performance Computing Modernization Program Annual Meeting, Nashville, June 27-30, 2005.

AFOSR Workshop on Stratospheric Turbulence, AFRL, Hanscom AFB, May 24-26, 2005.

European Geophysical Union (EGU) Annual Meeting, Vienna, April 28, 2005.

Workshop on “Deterministic and Stochastic Navier-Stokes Equations”, American Institute of Mathematics, Palo Alto, March 14-18, 2005.

American Meteorological Society Annual Meeting, January 2008, New Orleans.

SIAM Conference on Mathematical and Computational Issues in the Geosciences, March 19-22, 2007, Santa Fe.

8th Annual WRF Users Workshop, National Center for Atmospheric Research, June 11-15, 2007, Boulder.